International Journal of Heat and Mass Transfer 253 (2025) 127540

Contents lists available at ScienceDirect

International Journal of Heat and Mass Transfer

journal homepage: www.elsevier.com/locate/ijhmt

Particle thermal radiation characteristics and model for solar biomass gasification: Considering the effects of reaction stages

Jinhong Yu, Shiquan Shan *, Guopei Jin, Shizhun Liu, Guijia Zhang, Zhijun Zhou

State Key Laboratory of Clean Energy Utilization, Zhejiang University, Hangzhou, China, 310027

ARTICLE INFO

Keywords:
Thermal radiation
Heat transfer
Solar-driven biomass gasification
Kramers-Kronig relation
Mie theory
Optical constant model

ABSTRACT

Solar-driven biomass gasification uses solar radiation to produce syngas, enabling efficient solar energy storage and integrated biomass energy conversion. The thermal radiation properties of biomass powders are crucial for heat transfer performance, gasification efficiency, and product quality. Therefore, the influence of these properties during the reaction stages requires further investigation. In this study, biomass samples from different reaction stages were prepared, and their transmittance characteristics within the solar radiation spectrum (0.4-2.5 μm) were experimentally measured. The changes in radiation absorption at various gasification stages were analyzed. By combining Kramers-Kronig dispersion relations with Mie theory, the refractive index and extinction coefficient of the materials were accurately determined. The effects of wavelength, reaction stage, and ash content on the optical parameters of biomass were summarized. Based on experimental data, a 6th-order optical constants model for biomass concentrated radiation gasification was developed, with a prediction error as low as 3.81×10^{-5}. The radiation case results showed that considering the variation in optical parameters during the reaction stages significantly affects radiative heat flux and radiation source term distribution in the reactor. Near the wall, the changes in forward heat flux and radiation source term reached 96% and 21.36%, respectively. This study reveals the mechanisms by which the reaction stage influences radiation heat transfer in solar-driven biomass gasification, establishing a general optical constants model. It provides crucial experimental data and a solid theoretical foundation for heat transfer performance and energy balance calculations in solar-driven biomass gasification processes.

1. Introduction

Global energy consumption has surged by over 60% in the past 30 years, with fossil fuels still making up more than 80% of the total [1]. This has caused annual carbon emissions to exceed 36 billion tons [2], contributing to severe environmental pollution [3]. As a result, the development of renewable and negative-carbon energy technologies [4], and negative-carbon energy technologies (BECCS) based on the synergy of biomass energy and solar energy hold great potential. Biomass resources are abundant and vast, with the current global potential for biomass energy use exceeding 100 EJ/yr [5]. As a clean, renewable, and carbon-neutral resource [6], biomass is gaining more attention [7]. Besides, solar energy is a vast and clean energy source, it also faces challenges such as intermittency and variability [8].

Solar-driven thermochemical technology is a method that uses solar energy to provide the required heat for chemical reactions, enabling efficient solar energy conversion. Gasification, a typical endothermic reaction, can convert biomass energy into high-quality syngas [9]. For example, entrained flow gasification of biomass is considered one of the most promising technologies [10]. However, it requires burning a portion of the biomass (20-30%) to supply the necessary energy for the reaction [11]. Solar-driven biomass gasification enables non-combustion gasification of biomass [12], achieving complementary coupling of two renewable energy sources and representing an important low-carbon and sustainable technological route [13].

Solar-driven gasification technology enables the storage of solar energy in the form of chemical energy and is an important pathway for solar fuel synthesis. It is gaining widespread attention [14]. Direct concentrated radiation-driven gasification efficiently utilizes the full solar spectrum, offering significant advantages such as low raw material combustion losses, high energy conversion efficiency, and high-quality product gas [15]. Zhang et al. [16] independently designed and built a solar thermochemical reaction system to perform solar radiation-driven carbon-containing material gasification experiments, discovering that

* Corresponding author.
E-mail address: shiquan1204@zju.edu.cn (S. Shan).

https://doi.org/10.1016/j.ijheatmasstransfer.2025.127540
Received 7 April 2025; Received in revised form 17 May 2025; Accepted 13 July 2025

the energy efficiency of the solar-driven catalytic gasification system was 23.8% higher than that of conventional radiation gasification. Chuayboon et al. [4] used solar energy to drive steam gasification of empty fruit bunch biomass, achieving an energy conversion efficiency of over 20%. Xu et al. [17] conducted solar-driven biomass cyclic gasification experiments using Fe_3O_4 as an oxygen carrier, with a carbon conversion ratio of 0.69 and an energy upgrade factor of 0.71 under optimal conditions. Wang et al. [18] designed a direct radiation solar gasification reactor, where under the radiation of a 9 kW solar simulator, the peak radiation flux reached 4426.3 kW/m^2, with H_2 accounting for 47.1% of the syngas and an energy upgrade factor of 1.15. Xin et al. [19] proposed a solar-biomass hybrid gasification system, with energy conversion efficiency and carbon efficiency of 73.06% and 66.81%, respectively, increasing by 10.45% and 54.25% compared to traditional gasification systems. Xu et al. [20] investigated the effect of solar concentration and reaction conditions on the system energy characteristics, finding that at 1000℃, the energy efficiency and exergy efficiency are 72.86% and 68.82%, respectively. Overall, solar-driven biomass gasification technology operates at higher reaction temperatures, offering higher energy upgrade factors and system energy conversion efficiency compared to conventional gasification and other solar thermochemical technologies, making it a promising renewable energy synergy technology.

The process of biomass particle absorption of solar radiation in solar-driven gasification is shown in Fig. 1. In the solar-driven gasification process [21], the thermal radiation properties of biomass particles directly affect their absorption of solar radiation [22], which in turn has a significant impact on the system heat transfer performance, gasification efficiency, and product quality. Therefore, thermal radiation properties are key parameters in numerical simulations for heat transfer and energy calculations in solar gasification. Dai et al. [23] conducted a numerical study on solar-driven gasification, determining the absorption and scattering coefficients of particles to be 0.9 and 1.1, respectively. Bellan et al. [24] performed CFD-DEM studies based on solar carbon particle gasification reactions, with the scattering factor set to 0.9 and emissivity set to 1. Boujjat et al. [25] developed a CFD model for a direct solar radiation jet bed biomass gasifier, assuming the particle emissivity to be 0.9, and used the weighted-sum-of-gray-gases model to calculate the absorption coefficients of the gas. Pozzobon et al. [26] modeled biomass gasification under high solar flux, assuming both biomass and char to be gray and diffuse materials, with absorptivity set to 0.37 and 0.88, respectively, and neglecting gas radiation. Ma et al. [27] conducted a detailed numerical simulation of a solar biomass steam gasification system, constructing a heat transfer model under a parabolic concentrator, but did not consider the impact of reactions on the biomass particle radiation properties. Guo et al. [28] simulated steam gasification of individual biomass char particles, assuming a constant emissivity of 0.75 for the biomass char particles. Liu et al. [29] determined the emissivity of beech char in solar-driven biomass gasification simulations to be 0.94. Yu et al. [30] investigated the thermal radiation properties of nine raw biomass pellet samples, specifically for solar gasification applications. Gerhardter et al. [31] conducted both numerical and experimental studies on the heat transfer characteristics of non-spherical coal slag particles, assuming a constant emissivity of 0.83 for the particles. In current studies on the thermal radiation properties of char particles during solar-driven gasification, the thermal radiation model is typically simplified to gray body absorption, with the absorption, and scattering coefficients treated as constants that do not vary with radiation spectra or gasification stages, neglecting the significant effect of the gasification process on the particle radiation properties.

During the gasification reaction, the physical and chemical properties of particles change, altering their absorption, scattering, and other thermal radiation properties, which directly affects the radiation heat transfer and energy calculations in the solar gasification process. Some studies have focused on the radiation properties of coal particles in combustion processes. Gronarz et al. [32] proposed a method for calculating the scattering and absorption characteristics of coal particles during gasification based on their burnout state, and studied the effects of particle size distribution, incident radiation, and optical constants on scattering and absorption characteristics. They selected both constant and wavelength-dependent optical constants, but did not consider the impact of reactions on optical parameters. Schiemann et al. [33] summarized studies on the emissivity of char particles, using Mie theory to investigate the relationship between char emissivity and temperature, and found that emissivity decreases with increasing temperature. Graeser et al. [34] found that in the 1.25-5.5 μm spectral range, the emissivity of coal particles decreases from 0.6 to 0.24 as the temperature increases from 1952 K to 2582 K. Zhong et al. [35] studied the evolution of surface reflectance of willow particles during solar pyrolysis, finding that reflectance first reached a minimum of 7.3%, then rebounded to 15.3%. Research on particle radiation properties has mainly focused on coal combustion, with limited attention to biomass gasification. Most studies have explored absorption, emission, and scattering characteristics, but few have examined how reaction stages affect biomass radiation properties. Changes in the physical and chemical properties of biomass particles during gasification alter their optical parameters, and assuming constant optical parameters in existing models hinders accurate prediction of particle radiation heat transfer in solar gasification. Therefore, further investigation in this area is critical.

Based on the above background, this paper conducts experimental

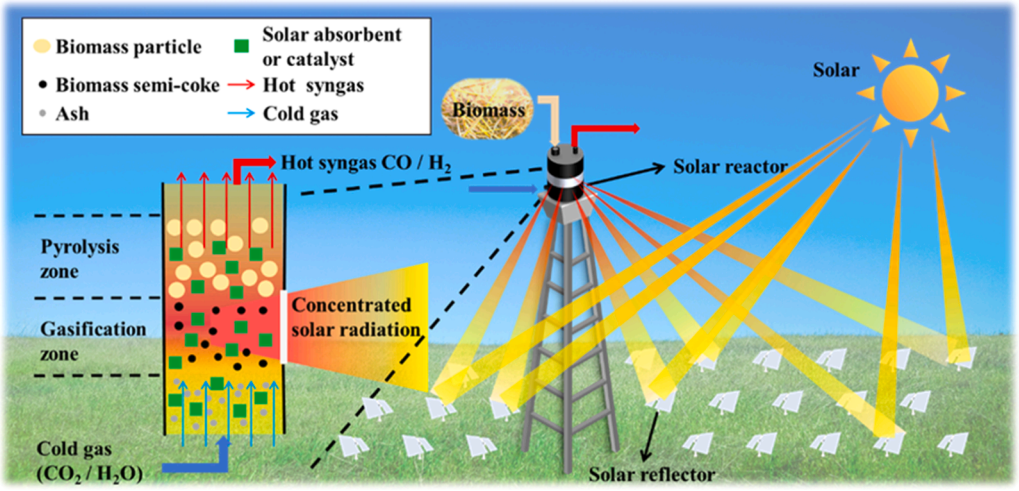

Fig. 1. Schematic of solar-driven biomass gasification.

and theoretical research on the thermal radiation properties of biomass particles during solar gasification and develops an optical constant model for biomass particles to fill the research gap in this field. The innovative work of this paper is mainly reflected in the following aspects: (1) The transmittance characteristics of three typical biomass material samples at different reaction stages were measured; (2) By combining the Kramers-Kronig relationship and Mie theory, the refractive index (n) and extinction coefficient (k) of samples at different reaction stages were inverted; (3) Based on the particle gasification process, a universal optical constant model for biomass particles was developed; (4) Heat transfer case analysis was performed to evaluate the effect of reaction stages on radiation heat transfer during biomass gasification. This study provides important experimental data and theoretical support for the thermal radiation properties of particles in solar biomass gasification, contributing to the application of this technology.

2. Experiments and method

2.1. Material and pretreatment

Agricultural and forestry waste is the main raw material utilized in commercial biomass gasification projects worldwide [36]. In this study, three typical biomass materials, namely wheat straw, bamboo, and rice hull, are selected as raw materials. The proximate and ultimate analyses of these raw materials are presented in Table 1.

A biomass chemical reaction experimental platform is used to prepare samples at different reaction stages of biomass gasification, as shown in Fig. 2. The semi-coke samples are heated at a constant rate of 20 K/min until reaching the target temperature, after which they are quickly cooled and removed through the sampling device. Samples from different gasification stages are prepared by gasifying semi-coke samples (600℃) for a certain period of time at 900℃ and then rapidly cooling them. Six sets of samples from different reaction stages are prepared in this study, as detailed in Table 2. The ash composition of wheat straw and rice hull is shown in Table 3.

2.2. Experiments of biomass materials

Before conducting the transmittance measurement, the samples must be carefully pretreated, and their density and particle size are measured. The particles should be processed to a uniform size of approximately 1 micron, with the assumption in the inverse calculation that they have identical diameters. Detailed procedures and results are provided in the Supplementary materials. Based on the experimental system designed to measure material transmittance across the ultraviolet-visible-near-infrared spectral range (Fig. 3), the transmittance of samples obtained at different reaction stages was measured [37]. In this experimental system, the tungsten halogen lamp serves as the light source. The collimating lens ensures alignment of the light between the receiving and emitting ends. The ultraviolet-visible spectrometer (AvaSpec-2048XL) and the near-infrared spectrometer (AvaSpec-NIR256-2.5-HSC-EV0) are used to capture transmitted light and analyze the spectral properties of the materials. Computer software records the data to measure spectral transmittance characteristics over the 0.4 to 2.5 μm spectral waveband. A light shield is used to prevent external light sources from affecting the transmittance measurement results. In this experiment, the samples are prepared using the tableting method and placed in a supporting structure, with the detailed transmittance measurement procedure described in the Supplementary materials.

2.3. Radiative characteristics theory

The optical characteristics of biomass directly affect its ability to absorb and utilize solar energy, significantly influencing heat transfer in the solar-driven gasification process. Mie scattering theory, based on the Maxwell's equations, is widely used to calculate the radiative characteristics of particles. Using the transmittance data, the Kramers-Kronig dispersion relation and Mie scattering theory can be combined to invert the optical constants of particles. The following sections will provide a detailed elaboration of these theories.

2.3.1. Mie theory

The Mie scattering formula describes the far-field solution of Maxwell's equations for an unpolarized plane electromagnetic wave incident on a homogeneous spherical particle. When a monochromatic plane electromagnetic wave with a wavelength λ interacts with an isotropic homogeneous spherical particle, the attenuation, scattering, and absorption of the particle can be expressed by the Mie theory.

$$Q_{ext}(m,\chi) = \frac{2}{\chi^2}\sum_{n=1}^{\infty}(2n+1)\mathrm{Re}\{a_n+b_n\} = \frac{4}{\chi^2}\mathrm{Re}\{S_0\} \tag{1}$$

$$Q_{sca}(m,\chi) = \frac{2}{\chi^2}\sum_{n=1}^{\infty}(2n+1)\left[|a_n|^2+|b_n|^2\right] \tag{2}$$

$$Q_{abs}(m,\chi) = Q_{ext}(m,\chi) - Q_{sca}(m,\chi) \tag{3}$$

Where Re represents the real part of the complex number. The size parameter χ is given by $\chi = \frac{\pi D}{\lambda}$, where D is the particle diameter and λ is the wavelength. S_0 is the forward scattering amplitude function, and a_n and b_n are the Mie scattering coefficients, calculated using the following formula:

$$a_n = \frac{\Psi_n'(m\chi)\Psi_n(\chi) - m\Psi_n(m\chi)\Psi_n'(\chi)}{\Psi_n'(m\chi)\xi_n(\chi) - m\Psi_n(m\chi)\xi_n'(\chi)} \tag{4}$$

$$b_n = \frac{m\Psi_n'(m\chi)\Psi_n(\chi) - \Psi_n(m\chi)\Psi_n'(\chi)}{m\Psi_n'(m\chi)\xi_n(\chi) - \Psi_n(m\chi)\xi_n'(\chi)} \tag{5}$$

$$\xi_n = \Psi_n - i\eta_n \tag{6}$$

Where $m=n+ik$ is the complex refractive index of the particle relative to the surrounding medium. Ψ_n and η_n are the Ricatti-Bessel functions, satisfying the following recursive relationship:

Table 1
Proximate analysis and ultimate analysis results of biomass feedstocks.

Material	Proximate Analysis						Ultimate Analysis			
	M%	A%	V%	FC%	Q_S (j/g)	C%	H%	N%	S%	O%
Wheat straw	9.93	29.44	48.9	11.73	12262	30.01	3.53	0.87	0.14	26.12
Rice hull	9.27	14.12	61.18	15.43	15356	38.14	4.43	0.41	0.26	33.37
Bamboo	9.08	0.84	75.41	14.67	17393	44.36	5.21	0.35	0.58	39.58
Wheat straw semi-coke (T_p=600℃)	2.94	64.3	4.22	28.54	10756	30.42	1.08	0.78	0.14	0.34
Rice hull semi-coke (T_p=600℃)	3.67	40.44	5.5	50.39	19049	53.17	1.48	0.44	0.13	0.67
Bamboo semi-coke (T_p=600℃)	5.37	4.14	11.8	78.69	30631	86.24	2.45	0.51	0.49	0.8

*M, Moisture; A, Ash; V, Volatiles; FC, Fixed carbon; Q_S, Heating quantity of bomb cylinder; C, Carbon; H, Hydrogen; N, Nitrogen; O, Oxygen; S, Sulfur.

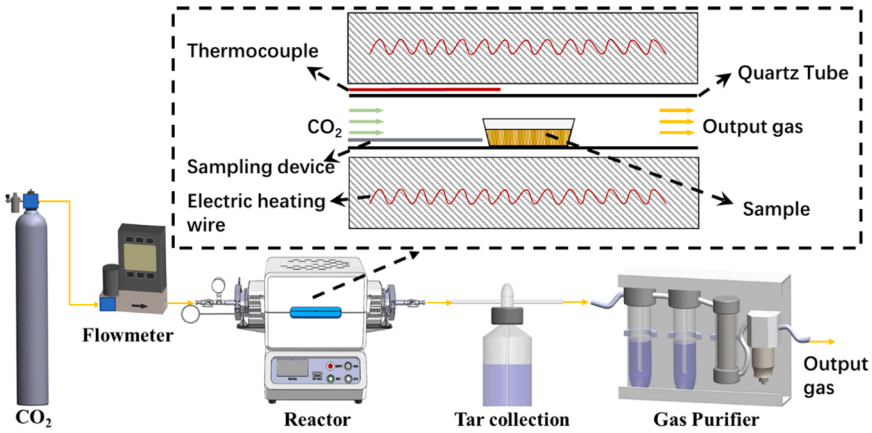

Fig. 2. Experimental platform for biomass thermochemical reaction.

Table 2
Working conditions of six sets of samples at different reaction stages.

Case	Sample	Pyrolysis temperature T_p/℃	Gasification temperature/℃	Gasification time/min
1	Wheat straw	30, 300, 400, 500, 600	—	—
2	Rice hull	30, 300, 400, 500, 600	—	—
3	Bamboo	30, 300, 400, 500, 600	—	—
4	Wheat straw semi-coke	600	900	10, 20, 40, 120
5	Rice hull semi-coke	600	900	20, 40, 80, 120
6	Bamboo semi-coke	600	900	10, 20, 40, 120

Table 3
Ash composition of wheat straw and rice hull.

	SiO_2	Al_2O_3	Fe_2O_3	CaO	MgO	K_2O	Na_2O
Wheat straw ash	87.96	1.57	1.76	0.44	2.32	2.19	0.59
Rice hull ash	92.05	0.5	0	0.15	1.27	3.27	1.61

$$\Psi_{n+1}(z) = \frac{2n+1}{z}\Psi_n(z) - \Psi_{n-1}(z) \tag{7}$$

$$\eta_{n+1}(z) = \frac{2n+1}{z}\eta_n(z) - \eta_{n-1}(z) \tag{8}$$

Where: $\Psi_{-1}(z) = \cos z$, $\Psi_0(z) = \sin z$, $\eta_{-1}(z) = -\sin z$, $\eta_0(z) = \cos z$.

According to Beer's law, when a beam of parallel light passes through a one-dimensional particle system, and the influence of multiple scattering is ignored, the spectral transmittance γ corresponding to a specific incident wavelength λ can be calculated by the following formula:

$$\gamma_\lambda = \exp\left(-\beta_\lambda s_p\right) = \exp\left[-s_p \cdot N_0 \int_{D_{\min}}^{D_{\max}} \frac{\pi}{4} D^2 P(D) Q_{ext,\lambda}(m,\chi) dD\right] \tag{9}$$

Where s_p is the path length of the particle system. N_0 is the total particle number. $P(D)$ is the particle size distribution density function. Therefore, when $P(D)$ size parameter χ and other geometric parameters are known, the complex refractive index m of the particle is directly related to the transmittance of the particle system.

2.3.2. *Inversion method for determining optical constants*

Since the complex refractive index m consists of both the refractive index n and the extinction coefficient k, additional conditions are required for its determination. A viable approach for inverting the optical constants of a material is to combine the experimentally obtained transmittance spectrum with the Kramers-Kronig dispersion relation and Mie theory. The Kramers-Kronig relation (Eq. (10) and Eq. (11)) establish a connection between the real part $n(\lambda)$ and the imaginary part $k(\lambda)$ of the causal function through an integral over the entire frequency

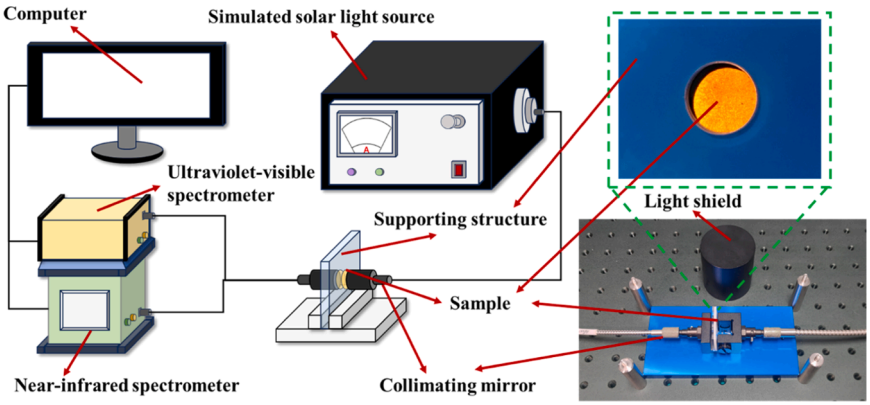

Fig. 3. Experimental equipment for measuring transmittance across the ultraviolet-visible-near-infrared spectral range.

range. This can then be combined with the particle system transmittance data to invert and calculate the complex refractive index m of the particle.

$$n(\lambda) = 1 + \frac{2\lambda^2}{\pi} \mathrm{P} \int_0^{\infty} \frac{k(\lambda_0)}{\lambda_0 (\lambda^2 - \lambda_0^2)} \mathrm{d}\lambda_0 \tag{10}$$

$$k(\lambda) = \frac{2\lambda}{\pi} P \int_0^{\infty} \frac{n(\lambda_0) - 1}{\lambda^2 - \lambda_0^2} d\lambda_0 \tag{11}$$

A particle system composed of particles with the same size is termed a homogeneous system. At a specific incident frequency ν, the single-frequency transmittance γ_ν of the particle system and the single-frequency attenuation factor $Q_{e,\nu}$ of a single particle are connected by the following relationship.

$$\gamma_\nu = \exp\left(-\frac{1}{4} \pi D^2 Q_{ext,\nu} N_0 \cdot s_p \right) \tag{12}$$

For a certain homogeneous particle system, the transmittance is equivalent to the attenuation factor, so the attenuation factor can be used as a simulation parameter. The complex function $A(\nu)$ is constructed that satisfies the Kramers-Kronig dispersion relation.

$$A(\nu) = i \cdot \chi^{-3} S_0 = Ar(\nu) + i \cdot Ai(\nu) \tag{13}$$

Where:

$$Ai(\nu) = \mathrm{Im}[A(\nu)] = \mathrm{Re}(S_0)\chi^{-3} \tag{14}$$

$$Ar(\nu) = \mathrm{Re}[A(\nu)] = -\mathrm{Im}(S_0)\chi^{-3} \tag{15}$$

The attenuation factor $Q_{ext,\nu}$ is related to the forward amplitude function by Eq. (1). By comparing Eq. (13) and Eq. (1), it follows that $Ai(\nu) = Q_{ext,\nu}/(4\chi)$. According to the Kramers-Kronig relation, the following formula is obtained:

$$Ar(\nu) = \frac{2}{\pi} P \int_0^{\infty} \frac{\Omega Ai(\Omega)}{\Omega^2 - \nu^2} d\Omega \tag{16}$$

Therefore, through the transmittance experiment and the Kramers-Kronig relation, the complex function $A(\nu)$ can be calculated. Assume that the function y_ν has the following form:

$$y_\nu = Ar(\nu) + i \cdot Ai(\nu) - i \cdot \chi^{-3} S_0 = f_1(\chi, m, \nu) = 0 \tag{17}$$

Corresponding to a certain frequency ν, when χ is known, the equation is simplified to a complex equation with the complex refractive index m is the variable, which is solvable. For each frequency ν, a similar equation can be obtained, and the spectral distribution of the complex refractive index m is determined.

Although directly using Mie theory to calculate the forward amplitude function S_0 is highly accurate, it is difficult to express it as an explicit equation for the complex refractive index m. Therefore, an approximate value m_0 must first be calculated, and then a complex equation (Eq. (17)) is solved using the chord method. The inversion calculation process is shown in Fig. 4, and further specific inversion process details are provided in the Supplementary materials. The explicit equation for the forward scattering amplitude function S_0 is calculated using the Rayleigh approximate scattering theory [38]:

$$S_0 = -i\chi^3 \left(\frac{m^2 - 1}{m^2 + 2} \right) \tag{18}$$

Based on this method to create a numerical program, the refractive index and extinction coefficient of the material in the full spectrum at different reaction stages can be obtained. It provides an important reference for the energy balance and heat transfer calculations in the solar-driven biomass gasification process.

2.4. Radiation transfer case analysis method

In this study, a one-dimensional radiation transfer model is set up for studying medium radiation heat transfer characteristics [39]. This model is employed to analyze the impact of the radiation characteristics of biomass at different reaction stages on the radiative heat transfer and radiation source term of the system, and to verify the importance of particle radiation characteristics.

2.4.1. Radiative transfer equation

The radiative transfer equation (RTE) is used in this study to solve the radiation heat transfer process of gas and particle media. The RTE describes the variation of radiation intensity along the propagation direction, as well as the effects of gas and particle absorption, emission and scattering on radiation intensity [40].

$$\frac{\partial I(s, \vec{s}^{\rightarrow})}{\partial s} = -(\kappa_g + \kappa_p + \sigma_p) I(s, \vec{s}^{\rightarrow}) + (\kappa_g + \kappa_p) I_b(s) + \frac{\sigma_p}{4\pi} \int_{\Omega_i = 4\pi} I(s, \vec{s}^{\rightarrow}) \Phi(s, \vec{s}^{\rightarrow}) d\Omega_i \tag{19}$$

Where $I(s, \vec{s}^{\rightarrow})$ is the radiation intensity at position s in the direction $\vec{s}^{\rightarrow}$. κ_g is the absorption coefficient of the gas mixture. κ_p is the

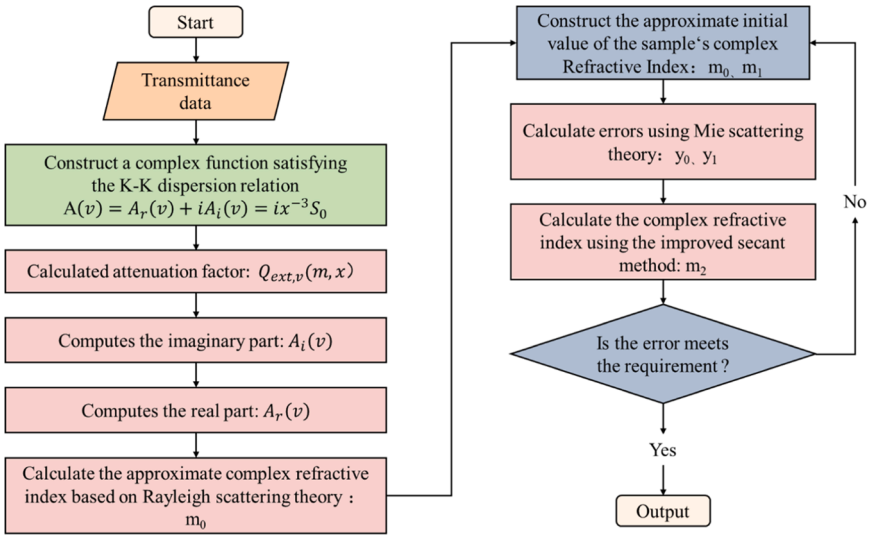

Fig. 4. Flowchart of optical parameter inversion.

absorption coefficient of the particles. σ_p is the scattering coefficient of the particles. $I_b(s)$ is the blackbody radiation intensity at position s. $\Phi(s, \vec{s}^{\rightarrow})$ is the scattering phase function, representing the energy fraction scattered from the incident direction to the exit direction. Ω_i is the solid angle.

The discrete ordinate method (DOM) is used to calculate the RTE [41] and the radiation heat transfer characteristics. In the process of solving RTE, the particle radiation characteristics are calculated using the material properties obtained in this study combined with Mie theory, while radiation characteristics of the gas medium are calculated using the SNB model [42]. The SNB model has been shown to produce results that closely match those derived from the LBL method based on the HITEMP2010 database [43]. The SNB model divides the spectrum into narrow bands with a width of 25 cm^{-1}. The isothermal isotropic average gas transmittance in the band is expressed as:

$$\overline{\tau}_v = \exp\left[-\frac{2\overline{\gamma}}{\overline{\delta}}\left(\sqrt{1+\frac{XPL\overline{k}\overline{\delta}}{\overline{\gamma}}}-1\right)\right] \tag{20}$$

Where the parameters $\overline{k}$ and $\overline{\delta}$ are obtained from the EM2C database [42].

In the radiation case analyzed in this study, both the variation in biomass particle size across reaction stages and the particle size distribution are considered. The biomass particle size at each reaction stage is determined using the following equation:

$$D_{Biomass} = \left(\frac{6m_{Biomass}}{\pi\rho_{\text{Biomass}}}\right)^{\frac{1}{3}} \tag{21}$$

Where $D_{Biomass}$ is the diameter of sample particle. $m_{Biomass}$ is the mass of the sample particles. ρ_{Biomass} is the density of sample.

The particle size distribution is assumed to follow the Rosin-Rammler distribution, with the particle size distribution at each reaction stage expressed as:

$$P(D) = \frac{s_d}{D_m}\cdot\left(\frac{D}{D_m}\right)^{(s_d-1)}\exp\left[-\left(\frac{D}{D_m}\right)^{s_d}\right] \tag{22}$$

Where $P(D)$ is the probability density of particle size D. D_m is the maximum particle diameter. s_d is the diffusion factor, which describes the width of the particle size distribution. In this study, the diffusion parameter s_d=3.7955 is determined based on previous studies [32].

2.4.2. Radiation transfer cases

A one-dimensional radiation transfer model is used to simulate the temperature field inside an axisymmetric cylindrical reactor. It is assumed that the temperature distribution along the radial direction is a cosine function distribution (Eq. (23)) with an average temperature of 1200 K [44], and cases 1-5 are designed accordingly. This distribution can model the temperature profile in gasifiers, such as the entrained flow gasifier [45]. Building upon the cosine temperature distribution, the typical temperature characteristics of solar gasifiers are also considered. An axial asymmetric temperature distribution (Eq. (24)) is further selected [46], and cases 6, 7 and 8 are designed. The two temperature distributions are as follows:

$$T_1(x) = 1200 - 300\cos\left(\frac{2\pi x}{L}\right) \tag{23}$$

$$T_2(x) = \begin{cases} -60000\times\left(\frac{x}{L}-0.1\right)^2+1500,\ 0\le\frac{x}{L}\le 0.1 \\ -\frac{10000}{27}\times\left(\frac{x}{L}-0.1\right)^2+1500,\ 0.1\le\frac{x}{L}\le 1 \end{cases} \tag{24}$$

The radial length of the reactor is set to 1 meter, where L=0 and L=1 correspond to the two reactor walls. The positive direction of radiation transfer is defined in Fig. 5. The gas molar ratio (M=X_{H2O}/X_{CO2}) is selected as M=0.25 [47], and the CO fraction is set to 0.5. Eight cases are considered: two conventional gasification cases and six solar-driven gasification cases, as shown in Table 4. The primary distinction among the six solar gasification cases lies in the radiation characteristics of the

Table 4
Information of eight radiation transfer cases.

Case	Temperature distribution	Gasification type	Reaction stage	Sources of radiation characteristic parameters
Case 1	$T_1(x)$, Eq. (23)	Conventional gasification	Ignored	Q_{abs}=0.9, Q_{sca}=1.1 [23]
Case 2	$T_1(x)$, Eq. (23)	Solar gasification	Ignored	Q_{abs}=0.9, Q_{sca}=1.1 [23]
Case 3	$T_1(x)$, Eq. (23)	Solar gasification	X_D=0.5, X_G=0	The proposed model
Case 4	$T_1(x)$, Eq. (23)	Solar gasification	X_D=1, X_G=0.5	The proposed model
Case 5	$T_1(x)$, Eq. (23)	Solar gasification	Custom	The proposed model
Case 6	$T_2(x)$, Eq. (24)	Conventional gasification	Ignored	Q_{abs}=0.9, Q_{sca}=1.1 [23]
Case 7	$T_2(x)$, Eq. (24)	Solar gasification	Ignored	Q_{abs}=0.9, Q_{sca}=1.1 [23]
Case 8	$T_2(x)$, Eq. (24)	Solar gasification	Custom	The proposed model

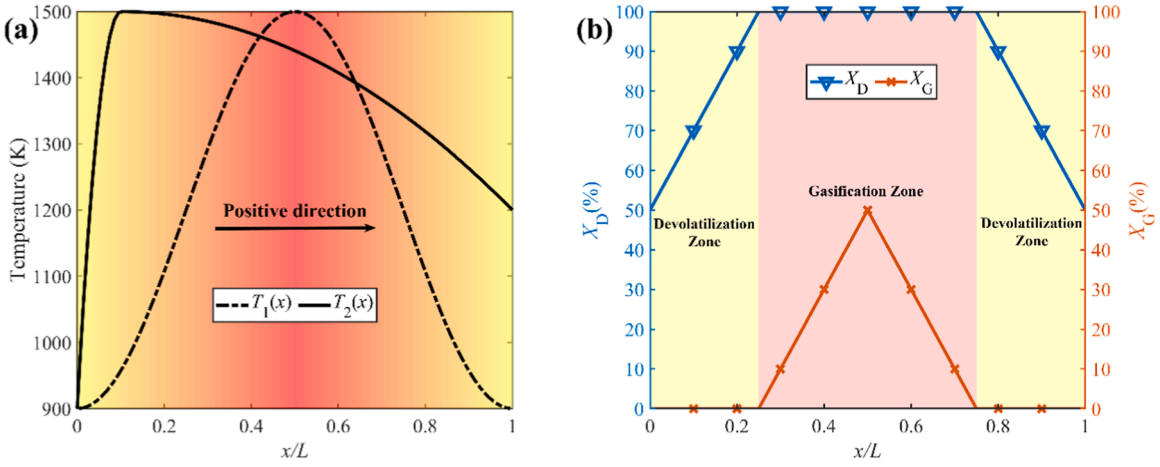

Fig. 5. (a) Radial temperature field and (b) reaction stage distribution of a symmetrical cylindrical reactor.

biomass particles. These radiation characteristics vary across different reaction stages, influencing their absorption of solar energy and the heat transfer performance within the reactor. In Case 5 and 8, it is assumed that the reaction stages (X_D and X_G) vary radially, reflecting the fact that biomass particles undergo different reaction stages along the radial direction of the reactor, as shown below:

$$X_D = \begin{cases} 0.5 + \dfrac{2x}{L}, & 0 \le \dfrac{x}{L} \le 0.25 \\ 1, & 0.25 \le \dfrac{x}{L} \le 0.75 \\ 2 - \dfrac{2x}{L}, & 0.75 \le \dfrac{x}{L} \le 1 \end{cases} \tag{25}$$

$$X_G = \begin{cases} 0, & 0 \le \dfrac{x}{L} \le 0.25 \\ \dfrac{2x}{L} - 0.5, & 0.25 \le \dfrac{x}{L} \le 0.5 \\ 1.5 - \dfrac{2x}{L}, & 0.5 \le \dfrac{x}{L} \le 0.75 \\ 0, & 0.75 \le \dfrac{x}{L} \le 1 \end{cases} \tag{26}$$

X_D represents the relative removal ratio of volatiles, which refers to the proportion of volatiles removed at different stages relative to the sample heated to 600℃. X_G denotes the semi-coke gasification conversion ratio, which is defined as the ratio of gasifiable substances in the semi-coke, excluding ash.

3. Results and discussion

3.1. Transmittance measurement results for biomass samples

This study measures the spectral transmittance of wheat straw, during four devolatilization stages, and through four gasification stages. Fig. 6(a) presents the transmittance measurement results for wheat straw samples across the five devolatilization stages. The results indicate that as the pyrolysis temperature (T_p) increases from 300℃ to 600℃, the relative removal ratio of volatiles are 23.3%, 80.5%, 94.5%, and 100%, respectively. By using the relative removal ratio to track the progress of biomass devolatilization, the reaction processes of various biomass samples can be unified, facilitating subsequent modeling of optical constants at different reaction stages.

As the pyrolysis temperature increases, the transmittance of wheat straw decreases, while its absorption characteristics strengthen. The devolatilization process has a more significant impact on transmittance at shorter wavelengths. At 500 nm, the spectral transmittance drops sharply from 89.45% (T_p=30℃) to 3.19% (T_p=600℃), while at 2400 nm, it decreases from 92.78% to 79.95%. This indicates that the devolatilization process more strongly affects spectral transmittance in shorter wavelengths, enhancing the sample absorption in this waveband.

Fig. 6(b) presents the transmittance measurement results of wheat straw samples at five gasification stages. The gasification conversion ratios of the wheat straw semi-coke samples are 0%, 32.1%, 44.8%, 69.4%, and 100%, respectively. Unlike the devolatilization process, transmittance during gasification decreases and then increases with the conversion ratio, suggesting that absorption characteristics strengthen initially and later weaken. At 500 nm, spectral transmittance remains stable between 1.04% and 5.48% during gasification, indicating strong absorption in the short-waveband. After complete gasification, the spectral transmittance of ash increases to 59.68% at 500 nm. At 2400 nm, spectral transmittance decreases from 79.95% to 11.26% and then increases to 81.28%, indicating that gasification mainly affects radiation characteristics at longer wavelengths.

Overall, during devolatilization and gasification processes, the absorption characteristics of wheat straw first increase and then decrease. This trend aligns with Zhong et al.'s findings on willow pellets [35]. The increase in carbon proportion enhances absorption during devolatilization, while the reduction in carbon and increase in ash during gasification weakens absorption. Thus, semi-coke with a higher carbon ratio is more suitable for receiving solar radiation in solar-driven biomass gasification systems, improving overall efficiency.

To study the effect of biomass composition on radiative properties, three biomass samples, wheat straw, bamboo, and rice hull, were selected, with ash contents of 29.4%, 0.84%, and 14.12%, respectively. Fig. 7(a), (b), and (c) illustrate the transmittance variation of these samples at pyrolysis temperatures of 30℃, 400℃, and 600℃. When T_p=30℃, wheat straw and rice hull exhibited high transmittance, around 90%. The microstructures of these samples (Fig. 8(a) and (d)) are composed of large, block-like structures with fewer voids, resulting in weak absorption. When T_p is 400℃ or 600℃, transmittance decreased significantly, especially at 600℃, where the spectral transmittance of all three samples in the 400-500 nm range fell below 5%. This reduction is due to the removal of volatiles at high pyrolysis temperatures, which increases the carbon and ash content of the semi-coke to 82.83-92.84%, forming abundant microscopic pores (Fig. 8(b) and (e)), which enhance radiation absorption.

Transmittance reduction correlates negatively with ash content.

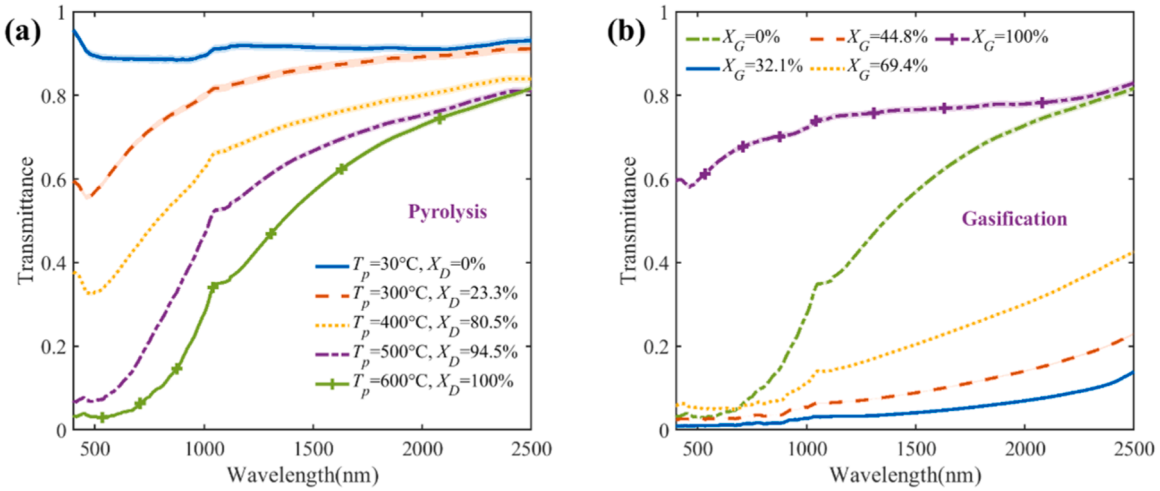

Fig. 6. Transmittance measurement results of wheat straw at different reaction stages. (a) Pyrolysis stage. (b) Gasification stage.

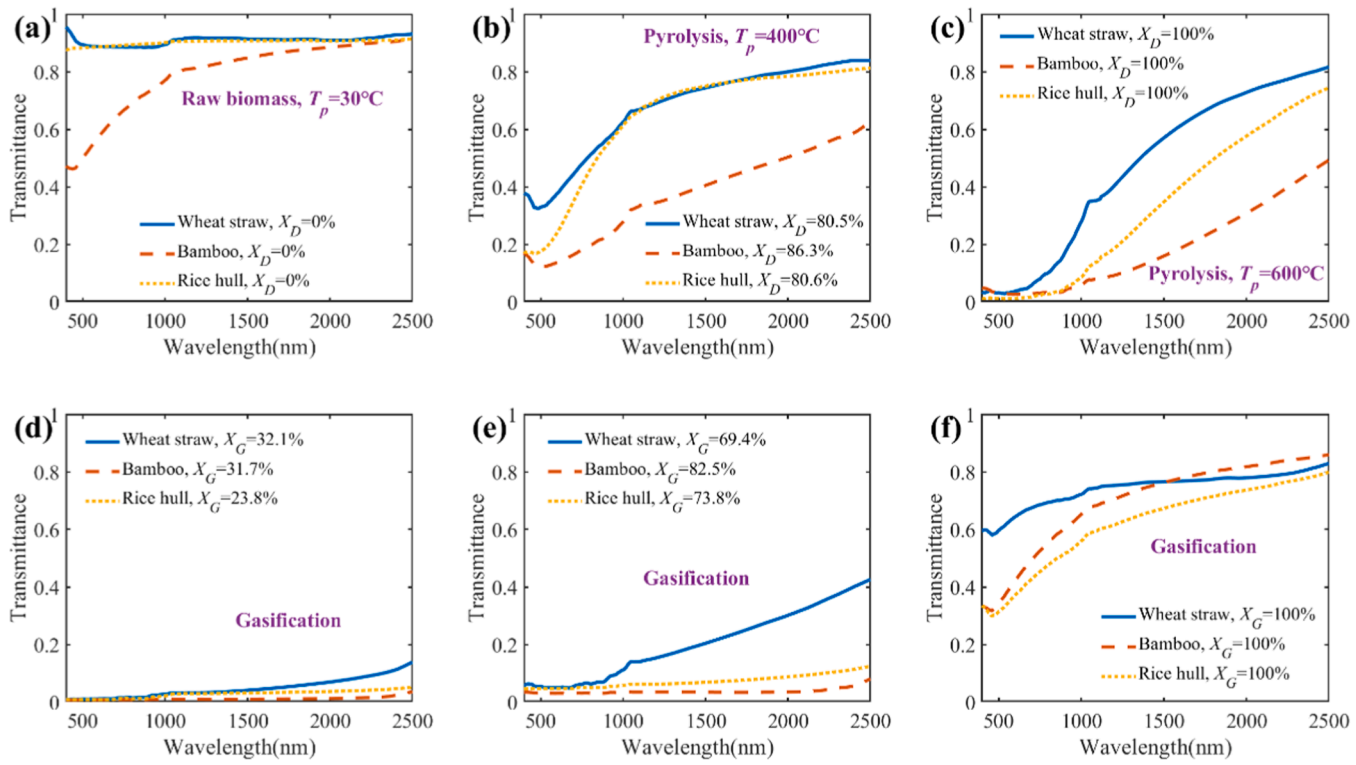

Fig. 7. Transmittance measurement results of three biomasses at different reaction stages. (a) Raw biomass at T_p=30℃. (b) Pyrolysis stage at T_p=400℃. (c) Pyrolysis stage at T_p=600℃. (d) Gasification stage at X_G=23.8%-32.1%. (e) Gasification stage at X_G=69.4%-82.5%. (f) Gasification stage at X_G=100%.

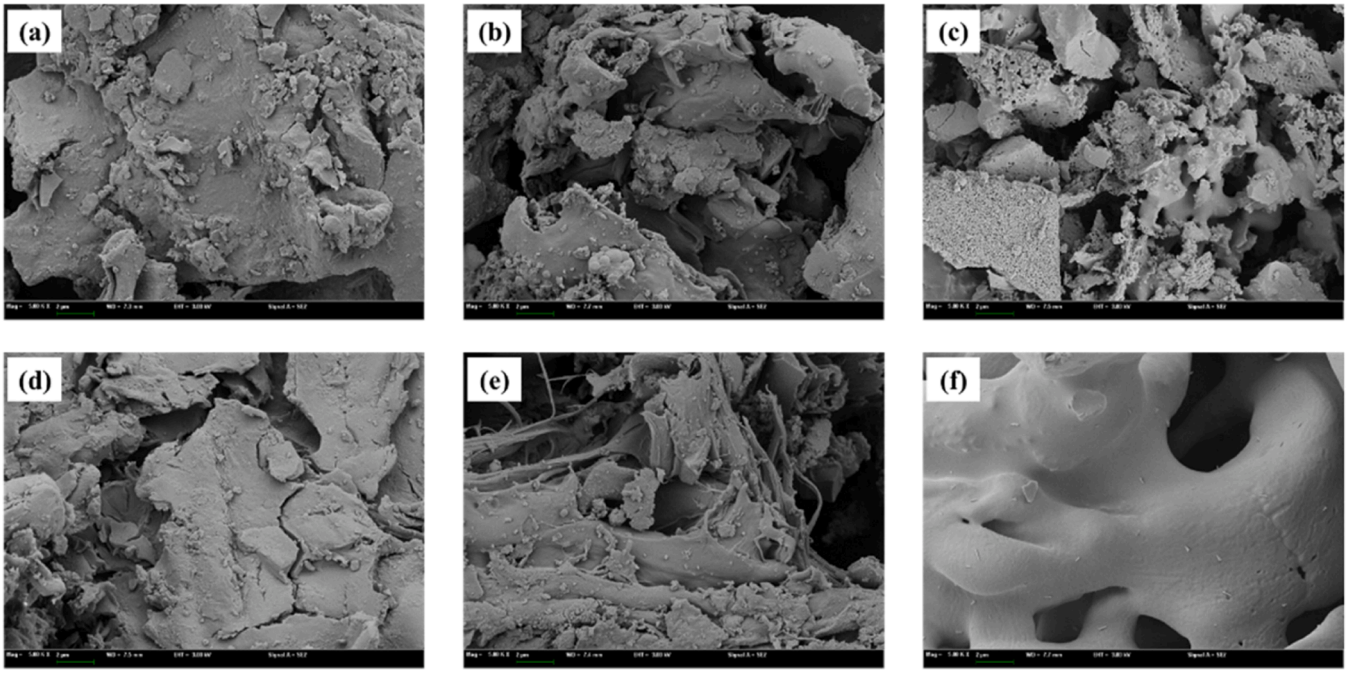

Fig. 8. SEM measurement results: (a) wheat straw, (b) wheat straw semi-coke (T_p=600℃), (c) wheat straw ash, (d) rice hull, (e) rice hull semi-coke (T_p =600℃), (f) rice hull ash.

Wheat straw, with the highest ash content (64.3%), has the lowest transmittance at 600℃. The spectral transmittance reduction is more pronounced in the short-wavelength range (400-1000 nm) than in the long-wavelength range (2000-2500 nm). The average reduction in transmittance for wheat straw, bamboo, and rice hull in the short-wavelength range is 80.7%, 58.2%, and 86.3%, respectively, compared to 14.4%, 50.0%, and 24.2% in the long-wavelength range, indicating that volatile removal has a more significant impact on short-wavelength radiation. Additionally, higher ash content results in smaller transmittance reductions in the long-wavelength range.

During gasification (X_G=23.8%-82.5%), bamboo and rice hull maintain low transmittance, with bamboo exhibiting the lowest, and

wheat straw the highest. This is related to ash content: higher ash in wheat straw leads to higher transmittance, while lower ash in bamboo enhances radiation absorption. Fig. 7(f) shows the transmittance of the ash of the three biomass samples after complete gasification. Wheat straw ash has higher spectral transmittance in 400-1500 nm than bamboo, while bamboo ash has higher spectral transmittance in 1500-2478 nm. Rice hull ash has the lowest transmittance across the entire spectrum, indicating stronger radiation absorption capacity. SEM analysis (Fig. 8(c) and (f)) shows that wheat straw ash has small pores and a rough surface, which enhances radiation absorption. In contrast, rice hull ash, with a smooth surface and high silica content, hinders gasification, thus resulting in greater residual char and enhanced radiation absorption. Therefore, to improve the radiative absorption characteristics of the sample in solar-driven biomass gasification, biomass raw materials with lower ash content and microstructures conducive to radiation absorption should be preferred.

3.2. Optical constant calculation results for biomass samples

Fig. 9(a) and (b) show the refractive index n and extinction coefficient k of wheat straw at different stages of devolatilization. As volatile matter is removed, the refractive index increases, rising from 1.017 to 1.19 at 1500 nm. The refractive index increases with wavelength when pyrolysis temperature is less than 400℃, ranging from 1.013 to 1.021 at wavelength of 400 nm, and from 1.0234 to 1.0659 at wavelength of 2478 nm. When T_p is 500℃ or 600℃, the refractive index initially increases and then decreases, with peaks of 1.125 at wavelength of 703 nm and 1.209 at wavelength of 675 nm, respectively. The extinction coefficient also generally increases with volatiles removal. For the sample with T_p=30℃, the extinction coefficient rises with wavelength, reaching 2.2×10^{-3} at 500 nm and 9.04×10^{-3} at 2478 nm. When T_p reaches 300℃ and 400℃, the extinction coefficient peaks at 485 nm and 530 nm, respectively, before decreasing. When T_p reaches 500℃ and 600℃, it shows higher extinction coefficients in the 400-1000 nm waveband, with a sharp decline as wavelength increases. In the 1000-2478 nm waveband, the extinction coefficient stabilizes around 0.02. Overall, both the n and k exhibit significant changes during the devolatilization process. As shown in Fig. 6(a), both the n and k generally increase with a corresponding decrease in transmittance.

Fig. 9(c) and (d) show the refractive index n and extinction coefficient k of wheat straw samples at different gasification stages. As the semi-coke gasification conversion ratio increases, the refractive index generally decreases. Additionally, the n at each gasification stage increases with wavelength. The k exhibits a clear wavelength dependence. In the range of 400-892 nm, the k increases with the gasification conversion ratios of semi-coke (32.1%, 44.8%, and 69.4%). However, in the 892-2478 nm waveband, the k decreases as the conversion ratio. For ash sample of wheat straw, the n ranges from 1.023 to 1.077, and the k ranges from 0.019 to 0.046, with overall optical properties stabilizing. In summary, during the volatile matter removal and gasification process of wheat straw, both n and k initially increase and then decrease, showing a negative correlation with transmittance. This trend suggests that as the gasification degree increases, the optical properties of the biomass particles undergo significant changes, particularly affecting the radiative properties at specific wavelengths.

Fig. 10 shows the trends in refractive index n for three biomass samples at different reaction stages. For samples that have not yet reacted, the n of rice hull is similar to that of wheat straw, with both increasing from 1.013 to 1.023 as the wavelength increases. The n of the bamboo sample is slightly higher, rising from 1.022 to 1.045 with increasing wavelength. In the pyrolysis (T_P = 400℃ and 600℃) and gasification (X_G = 23.8%-83.5%) stages, the n of rice hull samples lies between those of bamboo and wheat straw. Based on the proximate analysis data for the three biomass samples (Table 1), this phenomenon may be related to the ash content. As pyrolysis temperature increases, volatile matter is gradually released, and the main components of the sample transform into ash and char, with a lower n for ash. Since the ash content of rice hull is intermediate between that of bamboo and wheat straw, its n index remains between those of bamboo and wheat straw at all reaction stages. The n negatively correlates with the ash content of

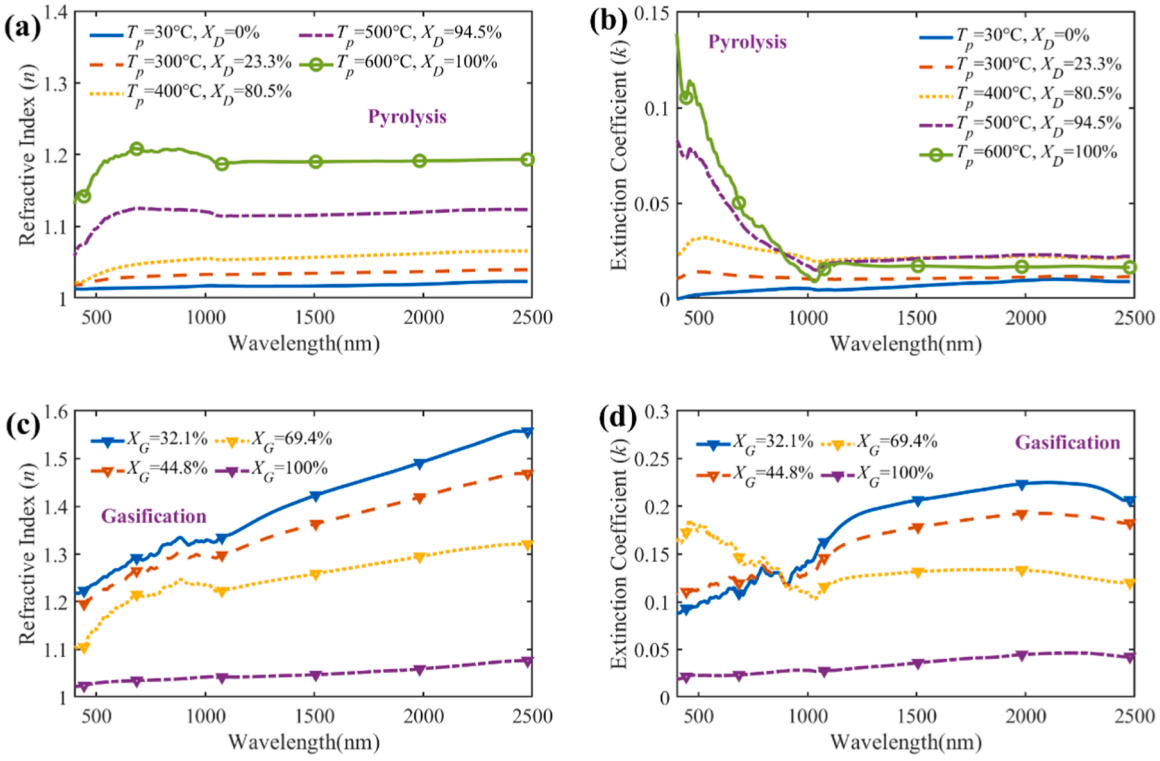

Fig. 9. Optical constants of wheat straw at different reaction stages. (a) n for the pyrolysis stages. (b) k for the pyrolysis stages. (c) n for the gasification stages. (d) k for the gasification stages.

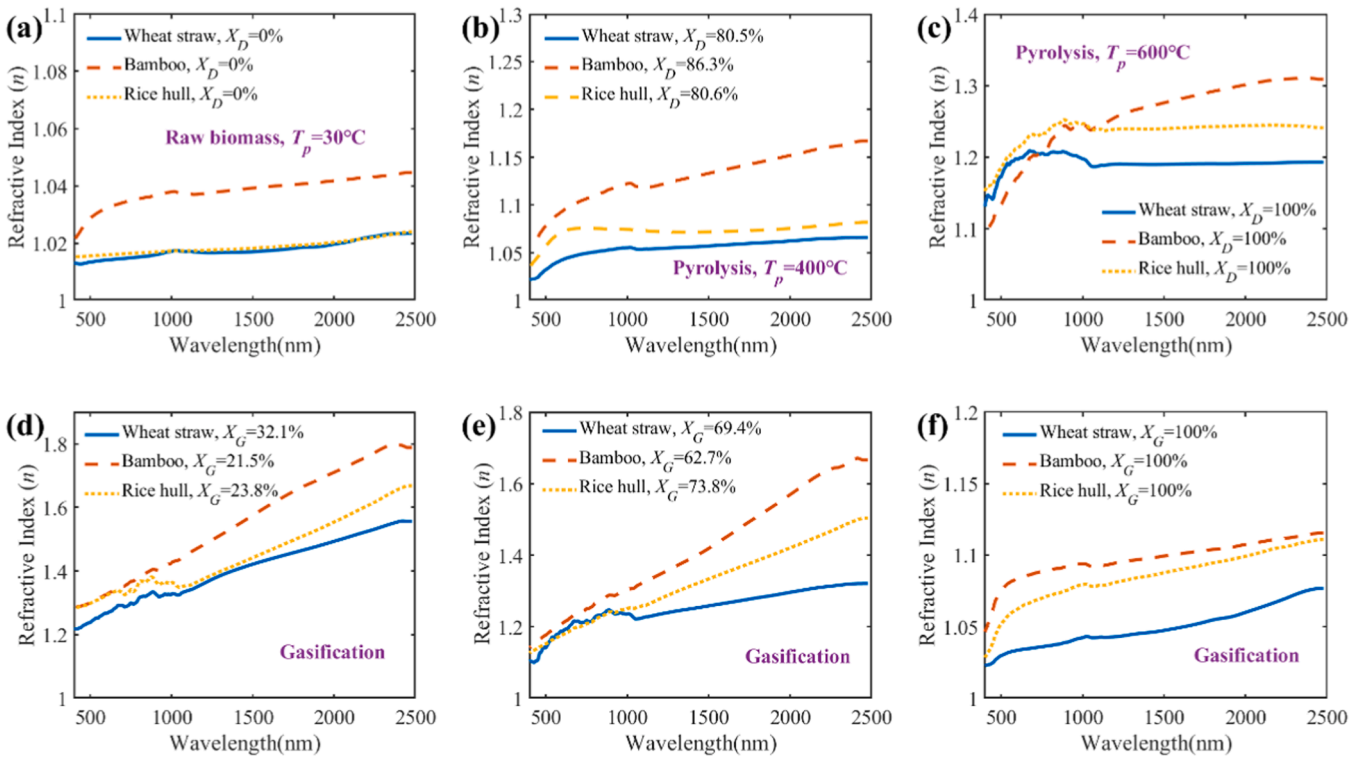

Fig. 10. Refractive index n of three biomass samples at different reaction stages. (a) Raw biomass at T_p=30℃. (b) Pyrolysis stage at T_p =400℃. (c) Pyrolysis stage at T_p =600℃. (d) Gasification stage at X_G=23.8%-32.1%. (e) Gasification stage at X_G=69.4%-82.5%. (f) Gasification stage at X_G=100%.

the sample. From a spectrum perspective, the n of all three samples increases with wavelength. Notably, at the gasification stage (X_G=23.8%-83.5%), the increase in n is more pronounced, indicating that wavelength has a positive correlation with n across all reaction stages, with this trend being more significant during gasification. Overall, the n of bamboo and rice hull increases and then decreases during volatile matter removal and gasification, a trend similar to that observed in wheat straw samples, confirming the applicability of these patterns to

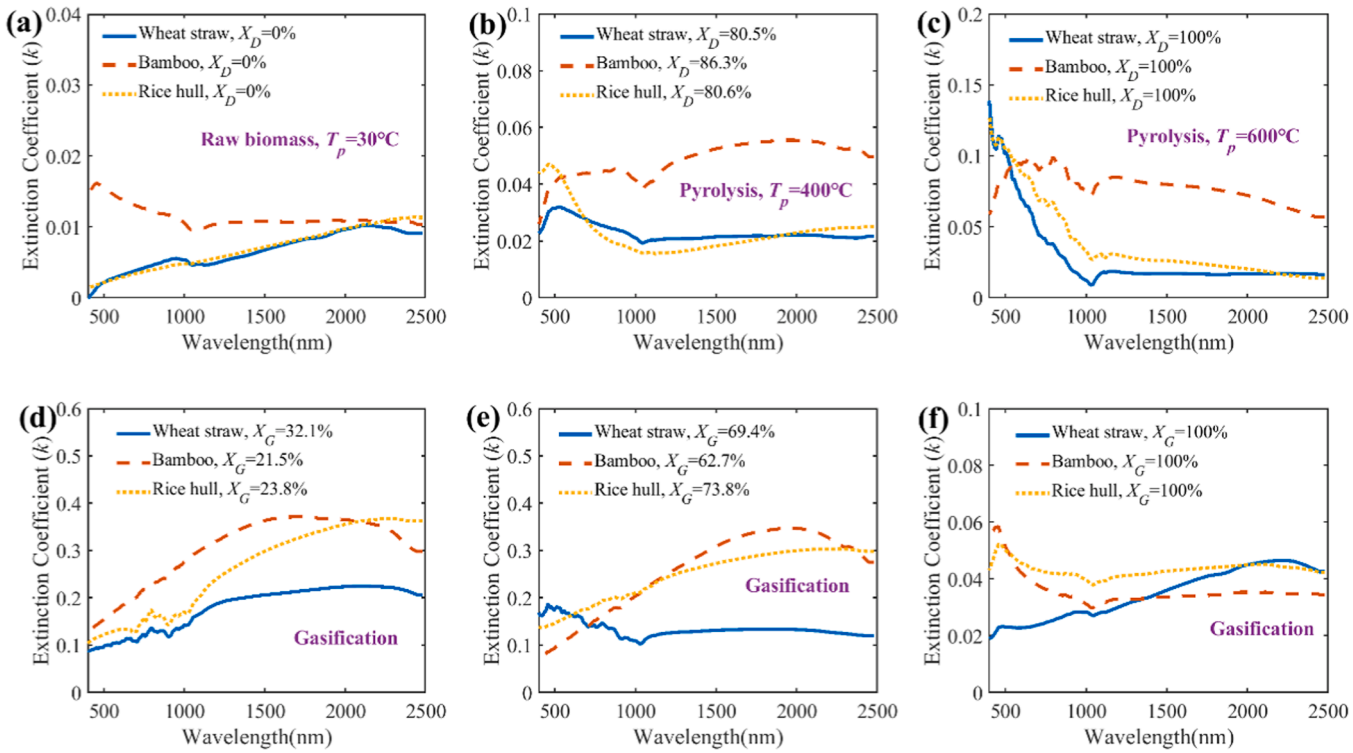

Fig. 11. Extinction coefficient k of three biomass samples at different reaction stages. (a) Raw biomass at T_p=30℃. (b) Pyrolysis stage at T_p=400℃. (c) Pyrolysis stage at T_p=600℃. (d) Gasification stage at X_G=23.8%-32.1%. (e) Gasification stage at X_G=69.4%-82.5%. (f) Gasification stage at X_G=100%.

different biomass types.

Fig. 11 shows the changes in extinction coefficient k for three biomass samples at different reaction stages. For samples that have not yet reacted, the k of rice hull is similar to that of wheat straw, increasing gradually from 0 to 0.01 as the wavelength increases. In contrast, the k of the bamboo sample ranges from 0.01 to 0.016. When T_p is 400℃ and 600℃, the k of rice hull is comparable to that of wheat straw, whereas that of bamboo is relatively higher. At the gasification stage (X_G=23.8%-83.5%), the k of both rice hull and bamboo samples is higher than that of wheat straw. This may be due to the higher ash content of wheat straw, which causes a decrease in its k during gasification, weakening its absorption characteristics. Further analysis of the k of ash samples (Fig. 11 (f)) indicates that, within the waveband of 400-2500 nm, the k of all three ash samples range from 0.02 to 0.06, with the rice hull ash sample having the highest k. Combined with the transmittance measurements of rice hull ash in Fig. 7(f), which show the lowest transmittance, it suggests that the extinction coefficient plays a dominant role in the absorption characteristics of the sample.

3.3. Construction of the biomass optical constants model

This section will develop a model for the optical constants of biomass. For the biomass devolatilization process, the relative removal ratio of volatiles, the sample ash content and the wavelength are chosen as independent variables to establish an optical constants model for the devolatilization process (Eq. (27)). To describe the change in optical constants with spectrum for biomass samples, a polynomial model $\sum_{i=1}^{N} a_i\lambda^{i-1}$ is used. In the devolatilization stage, where optical constants are influenced by both the relative removal ratio of volatiles matter and wavelength, a combined polynomial and exponential model $\sum_{i=1}^{N} b_i\lambda^{i-1}X_D^{f_1}$ is used to characterize the changes. Furthermore, considering that the optical constants differences between different biomass samples are mainly determined by the ash content, an additional model $\sum_{i=1}^{N} c_i\lambda^{i-1}(0.31-A_{sh})^{g_1}\cdot\left(d_iX_D^{i-1}\right)$ is built to reflect the impact of ash content on the optical constants, with the ash content ranging from 0 to 0.31. During the model prediction process, when only the three models mentioned above are used, the prediction error for the early devolatilization stage is relatively high. Therefore, a combined polynomial and exponential model $\sum_{i=1}^{N} e_i\lambda^{i-1}(1-X_D)^{f_2}\cdot A_{sh}{}^{g_2}$ is introduced to optimize the prediction accuracy for optical constants at different stages.

For the semi-coke gasification process, semi-coke gasification conversion ratio, sample ash content, and wavelength are used as independent variables to establish an optical constants model for the gasification process (Eq. (28)). Since the effect of the gasification stage on the optical constants differs from the devolatilization stage and shows an initial rapid increase followed by a decrease, a double-exponential model $\sum_{i=1}^{N} b_i\lambda^{i-1}\times\left(1-(1-X_G)^{h_1}+h_2X_G^{h_3}\right)$ is used to describe the variation in optical constants during the gasification process. The rest of the model remains the same as in the devolatilization stage.

$$f(\lambda,X_d,A_{sh})=\sum_{i=1}^{N}\left(a_i\lambda^{i-1}+b_i\lambda^{i-1}X_D^{f_1}+c_i\lambda^{i-1}(0.31-A_{sh})^{g_1}\cdot\left(d_iX_D^{i-1}\right)+e_i\lambda^{i-1}(1-X_D)^{f_2}\cdot A_{sh}{}^{g_2}\right) \tag{27}$$

$$f(\lambda,X_g,A_{sh})=\sum_{i=1}^{N}\left(a_i\lambda^{i-1}+b_i\lambda^{i-1}\cdot\left(1-(1-X_G)^{h_1}+h_2X_G^{h_3}\right)+c_i\lambda^{i-1}(0.31-A_{sh})^{g_1}\cdot\left(d_iX_G{}^{i-1}\right)+e_i\lambda^{i-1}(1-X_G)^{h_4}\cdot A_{sh}{}^{g_2}\right) \tag{28}$$

In the model, N represents the order of the model, λ is the wavelength, and A_{sh} represents the ash content of the sample (T_p=30℃). The parameters a_i, b_i, c_i, d_i and e_i are the coefficients of the polynomial model for the i-th group. f_1 and f_2 are the exponential model parameters describing the influence of the relative removal ratio of volatiles, g_1 and g_2 are the exponential model parameters for the effect of ash content, and h_1 to h_4 are the parameters for the effect of the semi-coke gasification conversion ratio.

The model parameters are fitted using the least squares method. The fitting error is less than 1×10^{-4}, which is calculated using the following formula:

$$R_{Squared}\equiv\frac{\sum_{j=1}^{M}\left[f_{mea}-f_{model}(\lambda,X_D,X_G,A_{sh})\right]^2}{M} \tag{29}$$

The $R_{Squared}$ represents the fitting error, f_{mea} is the measured value of the parameters to be fitted, f_{model} is the model-calculated value of the parameters, and M is the total number of fitting points.

Fig. 12(a) and 12(b) show the optical constants predictive results for wheat straw samples at different devolatilization stages. The solid line represents the model-calculated values, while the different marker points represent the measured values. The solid lines match marker points well, indicating that the model effectively describes the optical constants characteristics. Additionally, the predictive results for two other types of biomass are provided in the Supplementary materials. Fig. 13(a) further shows the prediction errors of optical constants during the devolatilization stage for models of different orders (from 2nd to 6th order). As the order N increases from 2 to 6, the average prediction error for the refractive index n decreases from 2.21×10^{-4} to 1.11×10^{-4}, while the prediction error for the extinction coefficient k drops from 1.15×10^{-4} to 3.81×10^{-5}. Overall, the prediction error for k is significantly smaller than that for n, indicating better performance of the model in describing the extinction coefficient. This difference may be due to the fact that the extinction coefficient k of biomass samples during the devolatilization stage is inherently small, which results in a relatively lower prediction error.

Fig. 12(c) and 12(d) show the optical constants prediction results for wheat straw samples at different gasification stages. Fig. 13(b) compares the prediction errors of models from 2nd to 6th order for the refractive index n and extinction coefficient k. The results indicate that, as the order increases, the average prediction error gradually decreases. The error for the refractive index n decreases from 5.25×10^{-4} to 1.92×10^{-4}, while the error for the extinction coefficient k decreases from 9.68×10^{-4} to 3.06×10^{-4}. Compared to the devolatilization stage, the model prediction errors for the gasification process are generally larger, mainly due to the larger variations in optical constants during gasification, especially at the initial and final stages of gasification. During these stages, optical constants undergo rapid increases or decreases, making the model prediction more challenging and enhancing the error. Overall, the 6th-order model effectively models the optical constants of different biomass types, with an overall prediction error less than 3.1×10^{-4}, demonstrating the applicability and accuracy of this method for predicting the biomass optical constants during the gasification process. All specific parameters of the 6th-order model are provided in the Supplementary materials.

Furthermore, Mie theory is applied to calculate the absorption and scattering factors of individual biomass particles. By comparing the results obtained from optical constants models and experimental measurements, the accuracy of the model can be verified. Fig. 14(a) and (b) show the calculated absorption factors Q_{abs} for three biomass samples. The scatter marker points represent the absorption factors obtained experimentally, while the solid lines represent the values calculated using the proposed model. It can be seen quite high agreement between the two sets of data. During the devolatilization process, the Q_{abs} of the biomass particles gradually increases, enhancing their absorption ability. In the gasification process, the Q_{abs} first increase and then decrease, with a high absorption observed when the semi-coke gasification conversion ratio is between 0.2 and 0.8. Regarding different biomass, wheat straw with high ash content exhibits lower absorption characteristics,

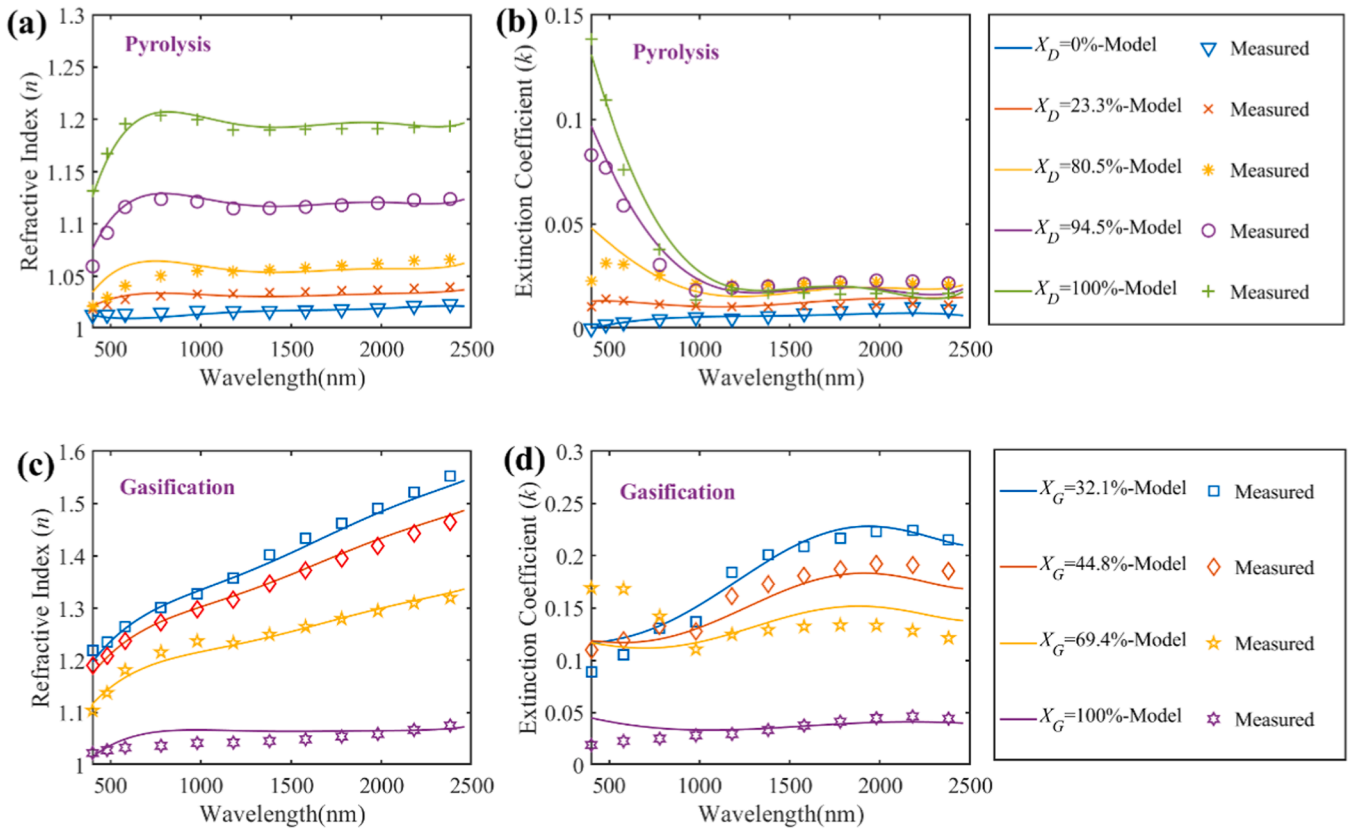

Fig. 12. Comparison of model-derived and measured optical constants (wheat straw). (a) n for the pyrolysis stages. (b) k for the pyrolysis stages. (c) n for the gasification stages. (d) k for the gasification stages.

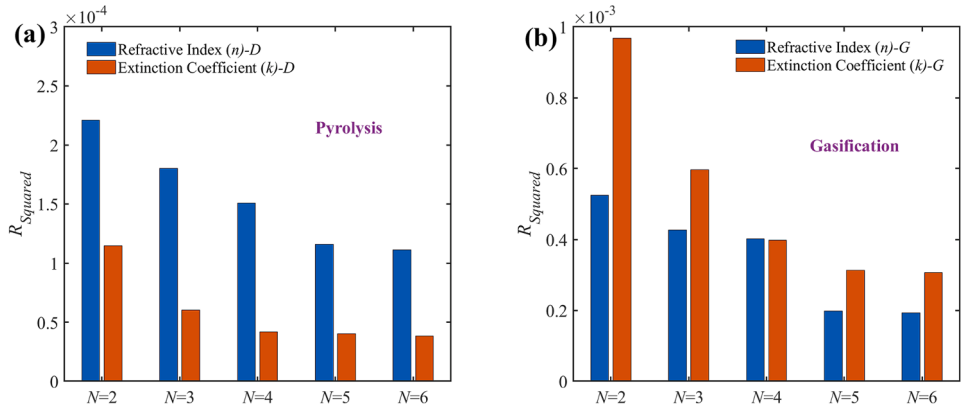

Fig. 13. Prediction errors for biomass optical constants in 2nd to 6th order models. (a) Pyrolysis stage. (b) Gasification stage.

while bamboo with low ash content shows greater absorption ability.

Fig. 14(c) and (d) presents a comparison of the average scattering factors Q_{sca} obtained from both the model and experimental data. From the figure, it can be seen that model calculated scattering factors align well with the experimental data. During the devolatilization process, the average scattering factor of the biomass samples increases with the X_D, with a more rapid increase observed in the X_D range from 0.8 to 1. In the gasification process, the scattering factors show an initial rapid increase followed by a gradual decrease. Overall, the differences in the average scattering factors between the three biomasses are small, indicating that biomass type has a significant impact on the absorption factor, but only a minor effect on the scattering factor.

3.4. Analysis of radiation heat transfer cases

Fig. 15(a) shows the calculated radiative heat flux under five different operating conditions. For conventional gasification (Case 1), the radiative heat flux inside the reactor primarily transfers from the central region toward the side walls, as defined by the positive direction in Fig. 5(a). In contrast, under solar-driven gasification conditions, the high-intensity solar concentrated radiation introduced from the side walls causes a significant change in the direction of the radiative heat flux near the wall regions. In the x/L range of 0-0.5, the radiative heat flux is transmitted from the wall (x/L=0) and the reactor axis (x/L=0.5) toward the heat flux equilibrium point. For different solar-driven gasification conditions, the heat flux equilibrium points are as follows, Case 3: x/L=0.149, Case 4: x/L=0.182, Case 5: x/L=0.327, indicating that

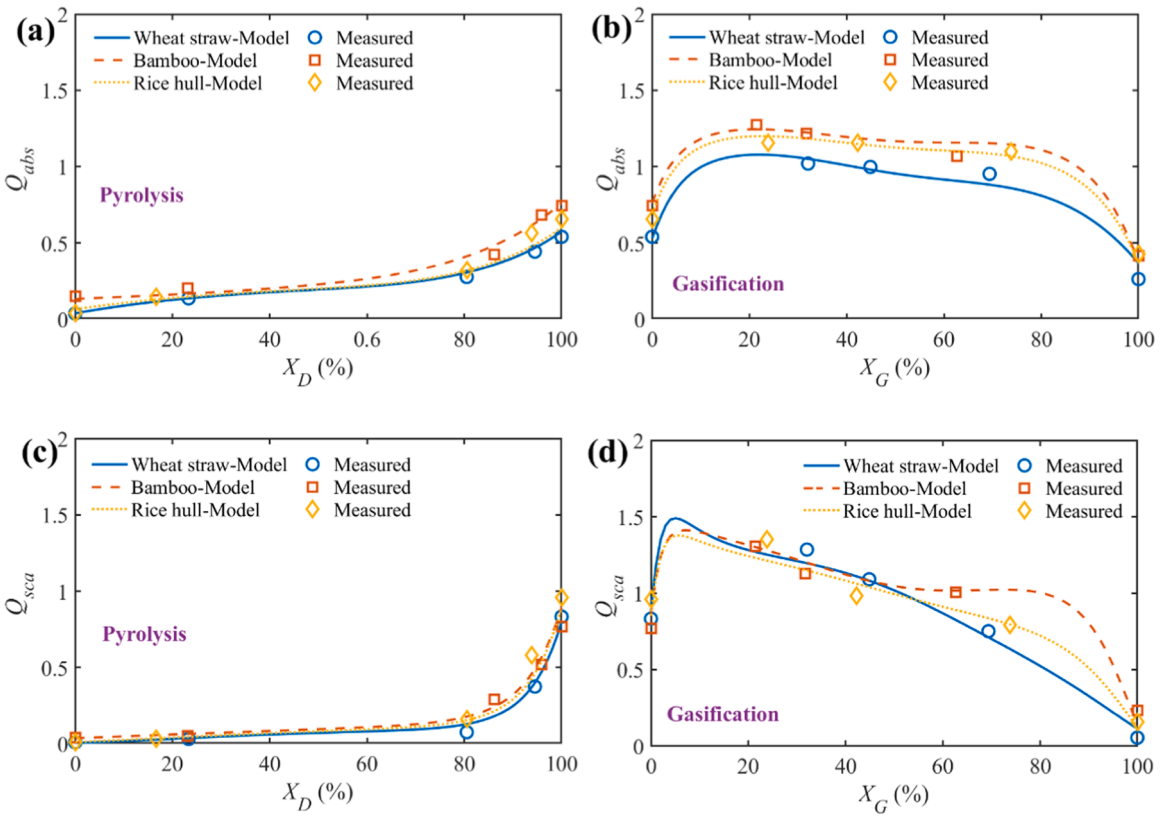

Fig. 14. Comparison of average absorption and scattering factors calculated from model (solid lines) and experimental data (scatter points). (a) Q_{abs} for the pyrolysis stages. (b) Q_{abs} for the pyrolysis stages. (c) Q_{sca} for the gasification stages. (d) Q_{sca} for the gasification stages.

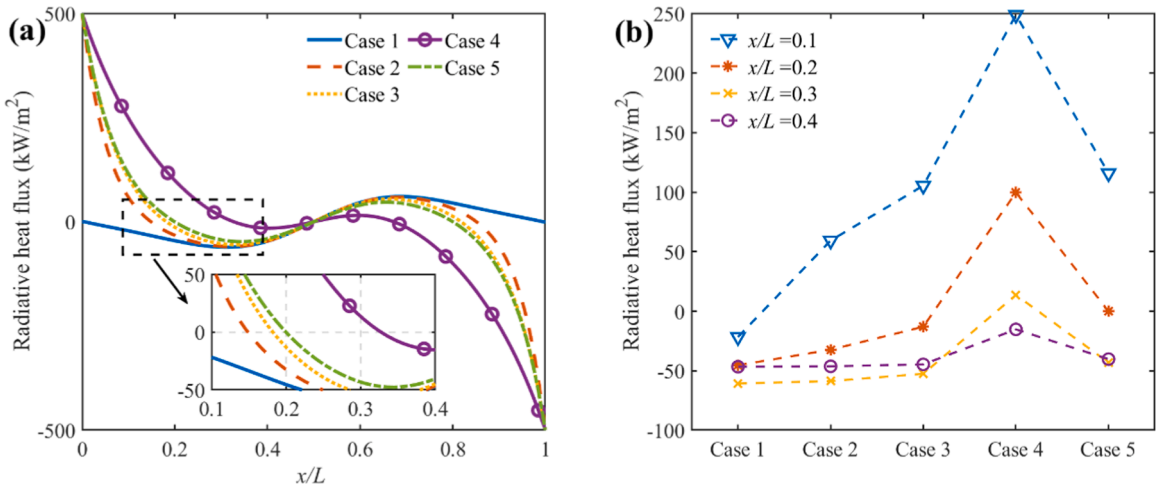

Fig. 15. Effect of bamboo radiation characteristics on radiative heat flux during the path-length: (a) calculated radiative heat flux under five different operating conditions; (b) comparison of the radiative heat flux distribution at x/L = 0.1-0.4 for various operating conditions.

both the heat flux distribution and transfer path change with the operating conditions.

Fig. 15(b) further compares the heat flux distribution at x/L=0.1-0.4 for different operating conditions. Compared to the reference Case 2, the forward heat flux along x/L=0.1-0.4 calculated using the proposed model (Case 3, Case 4, and Case 5) is larger. Particularly at x/L=0.1, the forward heat flux in Case 3, Case 4, and Case 5 is increased by 46.25 kW/m^2, 189.54 kW/m^2, and 56.65 kW/m^2 (78%, 320%, and 96%) compared to Case 2. This suggests that the radiation parameters in the reference may have overestimated the absorption characteristics of biomass particles. The results further demonstrate that the radiative properties of biomass particles play a critical role in the radiative heat transfer inside a solar-driven gasification reactor. In particular, optimizing the selection of optical parameters for different reaction stages is crucial for accurately simulating the heat transfer during the solar-driven gasification process.

Fig. 16(a) illustrates the calculated radiation source terms for five different operating conditions. The radiation source term represents the radiative energy absorbed by a micro-unit, with positive values indicating that the absorbed radiation exceeds the emitted radiation. For conventional gasification (Case 1), the radiation source term is negative, reaching its lowest value at the reactor center (-2421 kW/m^3). This

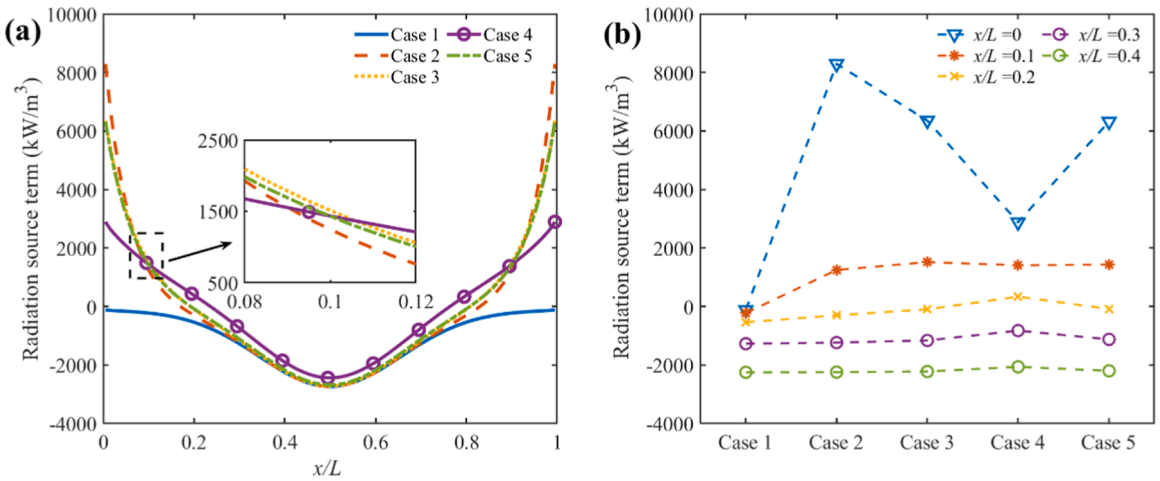

Fig. 16. Effect of bamboo radiation characteristics on radiation source term during path-length: (a) calculated radiation source term under five different operating conditions; (b) comparison of the radiation source term distribution at x/L = 0-0.4 for various operating conditions.

occurs because the highest temperature is at the center, causing the medium to emit the most radiation energy toward the side walls. In solar-driven gasification, the radiation source term near the side walls increases significantly, becoming positive for the micro-units. As the distance from the wall decreases, the radiation source term rises due to high-intensity solar radiation, which causes the medium near the walls to absorb more energy, increasing the radiation source term. Around the reactor axis (L=0.4-0.6 m), the radiation source term remains negative, similar to conventional gasification conditions, indicating that solar radiation primarily affects heat transfer near the wall region but has a weaker effect near the axis.

Fig. 16(b) compares the radiation source term along x/L=0-0.4 for different operating conditions. At x/L=0, the radiation source term for Case 2 reaches 8295 kW/m^3, while for Cases 3, 4, and 5, the values are 6355 kW/m^3, 2879 kW/m^3, and 6322 kW/m^3, respectively—lower than for Case 2. Along x/L = 0.1-0.4, the radiation source terms for Cases 3, 4, and 5 are higher. For example, at x/L = 0.1, the values for Cases 3, 4, and 5 are 21.36%, 12.82%, and 14.60% higher than for Case 2, respectively, indicating that these conditions absorb more energy. This confirms that the radiative properties of biomass samples significantly influence radiation transfer within the reactor. At x/L=0.1, the radiation source term curve for Case 4 intersects those for Cases 2, 5, and 3, as Case 4 has lower absorption near the side-wall region (x/L=0-0.1), allowing more concentrated radiation to reach the reactor axis (x/L=0.5), resulting in a higher radiation source term in the x/L=0.1-0.4 range. Fig. 17 shows the radiative transfer characteristics for cases 6, 7 and 8 under the temperature distribution $T_2(x)$. At x/L=0.1, the radiative transfer fluxes for Case 6, 7, and 8 are -73.56 kW/m^2, 6.74 kW/m^2, and 63.65 kW/m^2, respectively, while the radiation source terms are -3130.6 kW/m^3, -1521.79 kW/m^3, and -1360.24 kW/m^3, respectively. These results indicate that solar radiation significantly affects heat transfer near the window, and the differing thermal radiation characteristics of the particles result in a discrepancy of over 56.91 kW/m^2 in the radiative transfer flux. Therefore, the thermal radiation characteristics of biomass particles are essential for optimizing radiation transfer and energy balance in solar-driven gasification processes.

4. Conclusion

This study investigates the thermal radiation characteristics of particles during solar-driven biomass gasification, focusing particularly on the impact of the reaction stage and biomass composition. Biomass samples at different reaction stages were experimentally prepared, and their transmittance in the solar radiation spectrum (400-2500 nm) was measured. Based on the spectral transmittance data, the optical constants $n(\omega)$ and $k(\omega)$ were retrieved, and a universal biomass optical constants model suitable for solar-driven gasification processes was developed. An analysis of eight radiation heat transfer cases examined

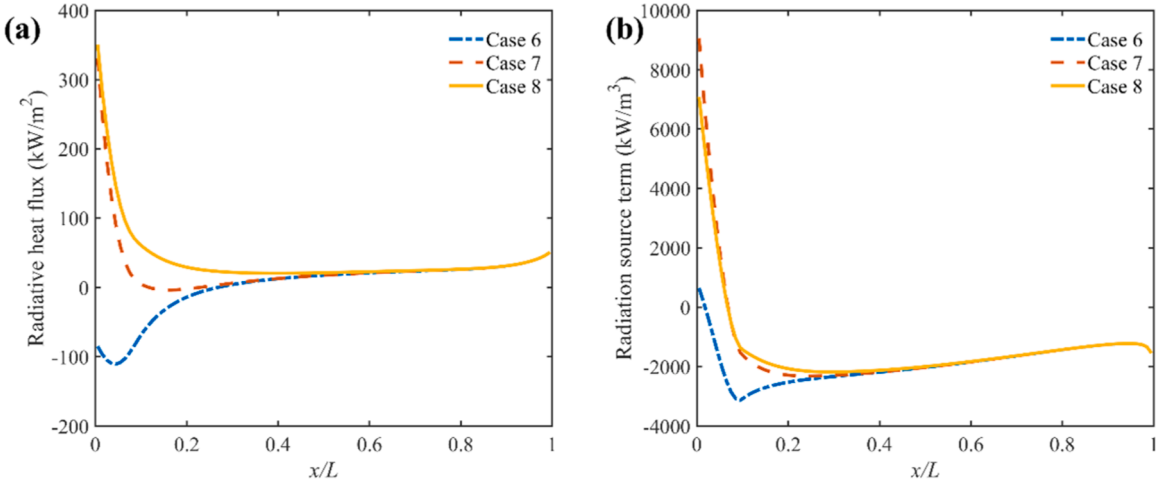

Fig. 17. Effect of bamboo radiation characteristics on radiative heat transfer during path-length with temperature distribution $T_2(x)$: (a) radiative heat flux, (b) radiation source term.

the effect of particle radiation properties on radiative heat transfer. The main conclusions are as follows:

(1) Radiation characteristics of biomass particles vary significantly with the reaction stage. During the devolatilization process, as the pyrolysis temperature increases from 30℃ to 600℃, volatile components are removed, the carbon proportion increases, and numerous micro-pores form, enhancing radiation absorption. For wheat straw samples, the spectral transmittance at short wavelengths (500 nm) dropped from 89.45% to 3.19%, indicating a significant increase in absorption. During the gasification process, the spectral transmittance first decreases and then increases, particularly at longer wavelengths (2400 nm), where transmittance decreased from 79.95% to 11.26% and then recovered to 81.28%. This suggests that absorption properties are enhanced in the early gasification stage, while the increased ash content in the later stage reduces absorption. Semi-coke with a higher carbon proportion has higher absorption efficiency, making it more suitable for solar-driven biomass gasification.

(2) Ash content is a key factor influencing the biomass radiative properties. Among the investigated biomass, bamboo has the highest absorption capability, followed by rice hull, while wheat straw has the lowest. This is inversely correlated with their ash content (bamboo: 0.84%, rice hull: 14.12%, wheat straw: 29.4%). The variation in spectral transmittance across wavelengths shows that wheat straw experiences a reduction of 80.7% in the short wavelength range (400-1000 nm), which is larger than the 14.4% reduction observed in the long wavelength range (2000-2500 nm). This suggests that volatiles removal more strongly affects short-wavelength radiation, and that higher ash content weakens the absorption in the longer-waveband. Wheat straw ash has the highest transmittance at 68.6% across the entire spectrum, which is 16.2% higher than rice hull ash. This is due to its more porous structures that facilitate gasification process. Biomass with low ash content and a microstructure conducive to radiation absorption can improve gasification efficiency.

(3) Reaction stage, ash content, and wavelength are the key factors affecting biomass thermal radiation characteristics. Both the refractive index n and extinction coefficient k increased with devolatilization progress. The n of wheat straw increased from 1.017 to 1.19 at 1500 nm, and k increased significantly in the short-wavelength range (400-1000 nm). In the gasification stage, the n decreased with the increase in semi-coke gasification conversion ratio, while the k increased in the short-waveband (400-892 nm) and decreased in the longer-waveband (892-2478 nm), indicating that the effects of gasification on optical constants are wavelength-dependent. Ash samples showed stable n (ranging from 1.023 to 1.077) and k (ranging from 0.019 to 0.046). Overall, ash content negatively correlates with refractive index, and low-ash biomass exhibits greater absorption properties during gasification.

(4) The 6th-order biomass optical constants model developed from experimental data shows high accuracy. A biomass optical constants model for solar-driven gasification processes was constructed using a combination of polynomial and exponential functions, with key variables including reaction stage (X_D and X_G), wavelength, and ash content. This model effectively describes the changes in optical constants. The prediction errors for n and k in the devolatilization stage were as low as 1.11×10^{-4} and 3.81×10^{-5}, respectively, while in the gasification stage, the prediction errors were 1.92×10^{-4} and 3.06×10^{-4}, indicating high accuracy. Mie theory validation showed that the absorption and scattering factors calculated by the model closely match experimental data, with prediction errors of 2.4×10^{-4} and 3.7×10^{-4}, respectively. This model provides a reliable tool for predicting the optical characteristics of biomass particles in solar-driven gasification processes.

(5) Particle radiation characteristics significantly affect radiation heat transfer within the gasification reactor. The results of the radiation heat transfer case analysis show that considering the variation in optical parameters with the reaction stage can significantly impact the distribution of radiation heat flux within the reactor. Under solar-driven gasification conditions, high-intensity solar radiation causes a significant change in the direction of heat flux near the reactor walls, with the heat flux balance point shifting as the operating conditions. The model-based Cases indicate a significant increase in forward heat flux at x/L=0.1 compared to Case2. Specifically, Case 5 exhibited a 96% increase, suggesting that previous studies may have overestimated the absorption characteristics of the particles. It also shows a significant increase in radiation source terms near the wall region, while the central axis region is less affected by solar radiation. The radiation source terms calculated for Case3, 4 and 5 were 12.82%-21.36% higher than Case2 for x/L=0.1-0.4, further validating the importance of biomass radiation properties in heat transfer.

CRediT authorship contribution statement

Jinhong Yu: Writing – original draft, Visualization, Validation, Software, Methodology, Investigation, Formal analysis, Data curation. **Shiquan Shan:** Writing – review & editing, Supervision, Resources, Project administration, Methodology, Investigation, Funding acquisition, Formal analysis, Conceptualization. **Guopei Jin:** Validation, Software, Formal analysis, Data curation. **Shizhun Liu:** Writing – review & editing, Software, Data curation. **Guijia Zhang:** Software, Data curation. **Zhijun Zhou:** Resources.

Declaration of competing interest

The authors declare that they have no known competing financial interests or personal relationships that could have appeared to influence the work reported in this paper.

Acknowledgments

This work was supported by Natural Science Foundation of Zhejiang Province (LZ25E060001), National Natural Science Foundation of China (52206175), and Fundamental Research Funds for the Central Universities (2022ZFJH04).

Supplementary materials

Supplementary material associated with this article can be found, in the online version, at doi:10.1016/j.ijheatmasstransfer.2025.127540.

Data availability

Data will be made available on request.

References

[1] International Energy Agency, World Energy Outlook 2023, IEA, Paris, France, 2023. https://www.iea.org/reports/world-energy-outlook-2023.

[2] P. Friedlingstein, M. O'Sullivan, M.W. Jones, R.M. Andrew, L. Gregor, J. Hauck, C. Le Quéré, I.T. Luijkx, A. Olsen, G.P. Peters, Global carbon budget 2022, Earth Syst. Sci. Data 14 (2022) 4811–4900, https://doi.org/10.5194/essd-14-4811-2022.

[3] I. Vinothkanna, S. Roseline, K. Balamurugan, S. Jeeva, I. Augastin Santhiyagu, The effects of greenhouse gas emissions on global warming, in: M.R. Rahimpour (Ed.), Encyclopedia of Renewable Energy, Sustainability and the Environment, First Edition, Elsevier, Oxford, 2024, pp. 143–154, https://doi.org/10.1016/B978-0-323-93940-9.00216-4.

[4] S. Chuayboon, S. Abanades, Continuous solar-driven gasification of oil palm agricultural bio waste for high-quality syngas production, Waste Management 154 (2022) 303–311, https://doi.org/10.1016/j.wasman.2022.10.015.

[5] H. Haberl, T. Beringer, S.C. Bhattacharya, K.-H. Erb, M. Hoogwijk, The global technical potential of bio-energy in 2050 considering sustainability constraints, Curr. Opin. Environ. Sustain. 2 (2010) 394–403, https://doi.org/10.1016/j.cosust.2010.10.007.

[6] A. Milićević, S. Belošević, N. Crnomarković, I. Tomanović, A. Stojanović, D. Tucaković, Lei Deng, D. Che, Numerical study of co-firing lignite and agricultural biomass in utility boiler under variable operation conditions, Int. J. Heat. Mass Transf. 181 (2021) 121728, https://doi.org/10.1016/j.ijheatmasstransfer.2021.121728.

[7] S. Chu, A. Majumdar, Opportunities and challenges for a sustainable energy future, Nature 488 (2012) 294–303, https://doi.org/10.1038/nature11475.

[8] L. Wei, Z. Pan, S. Sun, Z. Yi, G. Li, L. An, A novel electro-assisted thermochemical reactor for conversion of CO_2/H_2O into solar fuels, Int. J. Heat. Mass Transf. 229 (2024) 125742, https://doi.org/10.1016/j.ijheatmasstransfer.2024.125742.

[9] Y. Wang, G. Li, Z. Liu, P. Cui, Z. Zhu, S. Yang, Techno-economic analysis of biomass-to-hydrogen process in comparison with coal-to-hydrogen process, Energy 185 (2019) 1063–1075, https://doi.org/10.1016/j.energy.2019.07.119.

[10] M. Dammann, U. Santo, D. Böning, H. Knoch, M. Eberhard, T. Kolb, Entrained flow gasification: pilot-scale experimental, balancing and equilibrium data for model validation, Fuel 382 (2025) 132809, https://doi.org/10.1016/j.fuel.2024.132809.

[11] Y. Fang, M.C. Paul, S. Varjani, X. Li, Y.-K. Park, S. You, Concentrated solar thermochemical gasification of biomass: principles, applications, and development, Renew. Sustain. Energy Rev. 150 (2021) 111484, https://doi.org/10.1016/j.rser.2021.111484.

[12] H. Weldekidan, V. Strezov, G. Town, Review of solar energy for biofuel extraction, Renew. Sustain. Energy Rev. 88 (2018) 184–192, https://doi.org/10.1016/j.rser.2018.02.027.

[13] X. Yang, D. Zhong, K. Zeng, J. Li, X. Chen, H. Yang, H. Chen, Performance analysis of a novel biomass thermochemical conversion cascade utilization system driven by concentrated solar energy, Energy (2025) 135803, https://doi.org/10.1016/j.energy.2025.135803.

[14] P.K. Ghodke, A.K. Sharma, A. Jayaseelan, K.P. Gopinath, Hydrogen-rich syngas production from the lignocellulosic biomass by catalytic gasification: A state of art review on advance technologies, economic challenges, and future prospectus, Fuel 342 (2023) 127800, https://doi.org/10.1016/j.fuel.2023.127800.

[15] H. Song, G. Yang, P. Xue, Y. Li, J. Zou, S. Wang, H. Yang, H. Chen, Recent development of biomass gasification for H_2 rich gas production, Appl. Energy Combust. Sci. 10 (2022) 100059, https://doi.org/10.1016/j.jaecs.2022.100059.

[16] Q. Zhang, S. Shan, J. Yu, Z. Zhou, K.H. Luo, Coal gasification process driven by concentrated solar radiation for carbon neutralization: reaction and energy characteristics, Chem. Eng. J. 450 (2022) 138286, https://doi.org/10.1016/j.cej.2022.138286.

[17] D. Xu, B. Wang, X. Li, Y.W. Cheng, W. Fu, Y. Dai, C.-H. Wang, Solar-driven biomass chemical looping gasification using Fe_3O_4 for syngas and high-purity hydrogen production, Chem. Eng. J. 479 (2024) 147901, https://doi.org/10.1016/j.cej.2023.147901.

[18] S. Wang, X. Zhu, Y. Liu, Z. Bai, Q. Liu, X. Huang, H. Wang, F. Jiao, Design and experimental study of solar-driven biomass gasification based on direct irradiation solar thermochemical reactor, Chem. Eng. J. 500 (2024) 157062, https://doi.org/10.1016/j.cej.2024.157062.

[19] Y. Xin, X. Xing, X. Li, H. Hong, A biomass–solar hybrid gasification system by solar pyrolysis and PV– Solid oxide electrolysis cell for sustainable fuel production, Appl. Energy 356 (2024) 122419, https://doi.org/10.1016/j.apenergy.2023.122419.

[20] Z. Xu, S. Shan, Q. Zhang, L. Miao, Z. Zhou, Energy characteristic of concentrated solar coal gasification system based on experiment and model analysis, Solar Energy 279 (2024) 112846, https://doi.org/10.1016/j.solener.2024.112846.

[21] Q. Wang, C. Wu, X. Wang, S. Sun, D. Cui, S. Pan, H. Sheng, A review of eutectic salts as phase change energy storage materials in the context of concentrated solar power, Int. J. Heat. Mass Transf. 205 (2023) 123904, https://doi.org/10.1016/j.ijheatmasstransfer.2023.123904.

[22] J.V. Briongos, J. Gómez-Hernández, M. Díaz-Heras, J.A. Almendros-Ibáñez, Generalized volumetric energy balance for directly irradiated bubbling fluidized beds, Int. J. Heat. Mass Transf. 236 (2025) 126313, https://doi.org/10.1016/j.ijheatmasstransfer.2024.126313.

[23] S. Dai, Z. Chang, C. Chang, J.S. Akhatov, X. Li, Numerical study on the directly-irradiated vortex reactor for solar CO_2 coal gasification, Sol. Energy 188 (2019) 573–585, https://doi.org/10.1016/j.solener.2019.06.035.

[24] S. Bellan, T. Kodama, K. Matsubara, N. Gokon, H.S. Cho, K. Inoue, Thermal performance of a 30 kW fluidized bed reactor for solar gasification: A CFD-DEM study, Chem. Eng. J. 360 (2019) 1287–1300, https://doi.org/10.1016/j.cej.2018.10.111.

[25] H. Boujjat, S. Rodat, S. Chuayboon, S. Abanades, Experimental and numerical study of a directly irradiated hybrid solar/combustion spouted bed reactor for continuous steam gasification of biomass, Energy 189 (2019) 116118, https://doi.org/10.1016/j.energy.2019.116118.

[26] V. Pozzobon, S. Salvador, J.J. Bezian, Biomass gasification under high solar heat flux: advanced modelling, Fuel 214 (2018) 300–313, https://doi.org/10.1016/j.fuel.2017.10.011.

[27] C. Ma, Y. Zhou, J. Wang, X. Li, Numerical study on solar spouted bed reactor for conversion of biomass into hydrogen-rich gas by steam gasification, Int. J. Hydrogen. Energy 45 (2020) 33136–33150, https://doi.org/10.1016/j.ijhydene.2020.09.120.

[28] L. Guo, J. Liu, Z. Wang, Y. Zheng, P. Dong, Numerical simulation on steam gasification of a single biomass char particle, Energy Procedia 105 (2017) 1166–1171, https://doi.org/10.1016/j.egypro.2017.03.489.

[29] Y. Liu, R. Pan, R. Ansart, G. Debenest, Numerical simulation of solar-driven biomass gasification by using ceramic foam, Proc. Saf. Environ. Prot. 184 (2024) 300–313, https://doi.org/10.1016/j.psep.2024.02.008.

[30] J. Yu, S. Shan, Q. Zhang, X. Wang, G. Jin, Z. Zhou, Thermal radiation characteristic parameters of biomass mixed feedstock for concentrating solar gasification reaction, Therm. Sci. Eng. Progr. 54 (2024) 102791, https://doi.org/10.1016/j.tsep.2024.102791.

[31] H. Gerhardter, M. Knoll, J. Raic, R. Prieler, M. Landfahrer, C. Hochenauer, P. Tomazic, H. Schroettner, In-flame spheroid formation from non-spherical slag particles – A numerical and experimental study, Int. J. Heat. Mass Transf. 151 (2020) 119412, https://doi.org/10.1016/j.ijheatmasstransfer.2020.119412.

[32] T. Gronarz, M. Habermehl, R. Kneer, Modeling of particle radiative properties in coal combustion depending on burnout, Heat. Mass Transf. 53 (2017) 1225–1235, https://doi.org/10.1007/s00231-016-1896-0.

[33] M. Schiemann, T. Gronarz, P. Graeser, J. Gorewoda, R. Kneer, V. Scherer, A correlation between char emissivity and temperature, Fuel 256 (2019) 115889, https://doi.org/10.1016/j.fuel.2019.115889.

[34] P. Graeser, M. Schiemann, Investigations on the emissivity of burning coal char particles: influence of particle temperature and composition of reaction atmosphere, Fuel 263 (2020) 116714, https://doi.org/10.1016/j.fuel.2019.116714.

[35] D. Zhong, Z. Chang, K. Zeng, J. Li, Y. Qiu, Q. Lu, G. Flamant, H. Yang, H. Chen, Solar pyrolysis of biomass - part II: the physicochemical structure evolution of char, Fuel 333 (2023) 126474, https://doi.org/10.1016/j.fuel.2022.126474.

[36] Ö. Tezer, N. Karabağ, A. Öngen, C.Ö. Çolpan, A. Ayol, Biomass gasification for sustainable energy production: A review, Int. J. Hydrogen. Energy 47 (2022) 15419–15433, https://doi.org/10.1016/j.ijhydene.2022.02.158.

[37] G. Zhang, S. Shan, H. Wu, J. Tian, Z. Cheng, Z. Zhou, Investigation on the radiative characteristics of ZnO-SiO_2 nanofluids in spectral splitting photovoltaic/thermal systems, Solar Energy Materials and Solar Cells 277 (2024) 113129, https://doi.org/10.1016/j.solmat.2024.113129.

[38] J.C. Ku, J.D. Felske, Determination of refractive indices of Mie scatterers from Kramers–Kronig analysis of spectral extinction data, J. Opt. Soc. Am. A, JOSAA 3 (1986) 617–623, https://doi.org/10.1364/JOSAA.3.000617.

[39] G. Jin, S. Shan, X. Wang, J. Yu, Z. Wang, Z. Zhou, New multi-parametrical pressurized WSGG model correlations for gaseous radiative heat transfer in high H_2O/CO_2 molar ratio conditions for sustainable fuel utilization, Int. J. Hydrogen. Energy 69 (2024) 173–183, https://doi.org/10.1016/j.ijhydene.2024.04.367.

[40] X. Wang, S. Shan, Z. Wang, Z. Zhou, K. Cen, Review on thermal-science fundamental research of pressurized oxy-fuel combustion technology, Front. Energy 18 (2024) 760–784, https://doi.org/10.1007/s11708-024-0931-y.

[41] G.B. Rybicki, Radiative transfer, J. Astrophys. Astronomy 17 (1996) 95–112, https://doi.org/10.1007/BF02702299.

[42] A. Soufiani, J. Taine, High temperature gas radiative property parameters of statistical narrow-band model for H_2O, CO_2 and CO, and correlated-K model for H_2O and CO_2, Int. J. Heat. Mass Transf. 40 (1997) 987–991, https://doi.org/10.1016/0017-9310(96)00129-9.

[43] H. Chu, M. Gu, J.-L. Consalvi, F. Liu, H. Zhou, Effects of total pressure on non-grey gas radiation transfer in oxy-fuel combustion using the LBL, SNB, SNBCK, WSGG, and FSCK methods, J. Quantit. Spectrosc. Radiat. Transf. 172 (2016) 24–35, https://doi.org/10.1016/j.jqsrt.2015.07.009.

[44] R. Johansson, K. Andersson, B. Leckner, H. Thunman, Models for gaseous radiative heat transfer applied to oxy-fuel conditions in boilers, Int. J. Heat. Mass Transf. 53 (2010) 220–230, https://doi.org/10.1016/j.ijheatmasstransfer.2009.09.039.

[45] M. Dammann, M. Mancini, T. Kolb, R. Weber, Thermal radiation at high-temperature and high-pressure conditions: comparison of models for design and scale-up of entrained flow gasification processes, Therm. Sci. Eng. Progr. 42 (2023) 101772, https://doi.org/10.1016/j.tsep.2023.101772.

[46] A. Z'graggen, A. Steinfeld, A. Steinfeld, Hydrogen production by steam-gasification of carbonaceous materials using concentrated solar energy – V. Reactor modeling, optimization, and scale-up, Int. J. Hydrogen. Energy 33 (2008) 5484–5492, https://doi.org/10.1016/J.IJHYDENE.2008.07.047.

[47] X. Wang, S. Shan, B. Zhang, G. Jin, J. Yu, Z. Zhou, Parametrical study on spectral radiation characteristics of solid fuel combustion medium for energy cascade utilization, Fuel 361 (2024) 130660, https://doi.org/10.1016/j.fuel.2023.130660.